6-23-2015

Surface Charge Regulation Effects on Fluidic Nanoscale Systems

Mark Fleharty

Mark E. Fleharty

Candidate

Nanoscience and Microsystems

Department

This dissertation is approved, and it is acceptable in quality and form for publication:

Approved by the Dissertation Committee:

Prof. Dimiter N. Petsev , Chairperson

Prof. Frank van Swol

Prof. Sang M. Han

Prof. Plamen Atanassov

Surface Charge Regulation Effects on Fluidic Nanoscale Systems

by

Mark E. Fleharty

B.S., Computer Science, University of New Mexico, 2000
M.S., Computer Science, University of New Mexico, 2010

DISSERTATION

Submitted in Partial Fulfillment of the
Requirements for the Degree of

Doctor of Philosophy
Nanoscience and Microsystems

The University of New Mexico

Albuquerque, New Mexico

May, 2015

Dedication

To my parents, Mike and Laura, and my brothers Reagan and Dillon, and my friends for their support and encouragement.

Acknowledgments

I would like to give special thanks to my advisors, Professor Dimiter Petsev, and Professor Frank van Swol for their support. They have really helped me grow as a scientist, and I will forever be in their debt. I'd also like to thank Professor Sang M. Han, and Professor Plamen Atanassov for serving on my committee.

I would like to thank my many mentors who have helped me along with my long journey towards the Ph.D. Professor Susan Atlas, Professor Deborah Evans, Professor Thomas Caudell, Professor Mansoor Sheik-Bahae, Dr. Michael Hasselbeck, Professor Mary Anne Nelson, Professor Maggie Werner-Washburne, Professor Mousumi Roy, Professor Joe Galewsky, Dennis Doherty, and Brad Carvey.

Bea Yu, Lynn Kercher, Eric Benner, Edward (Lee) Hobbs, Jonathan Carter Hebert, Dr. Bahman Zohuri, and Farhod Bahritdinov all helped me maintain my sanity while finishing this document. Thank you!

Surface Charge Regulation Effects on Fluidic Nanoscale Systems

by

Mark E. Fleharty

B.S., Computer Science, University of New Mexico, 2000
M.S., Computer Science, University of New Mexico, 2010

Ph.D., Nanoscience and Microsystems, University of New Mexico, 2015

Abstract

Electrostatic properties of fluidic nanoscale systems are of fundamental interest and play an important role in many engineering applications. Due to the large surface area to volume ratios of these systems, interfacial phenomena are of key importance to understanding their behavior. We present several studies of fluidic nanoscale systems using the Poisson–Boltzmann equation which treats the fluid as a continuum, and density functional theory of fluids which uses a statistical mechanical treatment of the fluid that includes finite-size effects. Chemical equilibria at the interface is accounted for by coupling these methods with charge regulating theory. The effects of charge regulation lead to several novel predictions about fluidic nanoscale systems including pH dependent conductivities, reduced stability of doped colloidal dispersions, and a dependence of the surface charge on the solvent structure.

Contents

List of Figures **x**

List of Tables **xviii**

Glossary **xix**

1 Introduction **1**

1.1 Background and Literature Overview 2

1.1.1 Continuum Approach – The Poisson Boltzmann Equation . . 2

1.1.2 Introduction to Charge Regulation 5

1.1.3 Statistical Mechanical Models Based on the Ornstein–Zernike Equation 7

1.1.4 Density Functional Theory of Electric Double Layers 8

1.2 Motivation 10

1.3 Brief outline of Dissertation 11

2 Effects of Charge Regulation on Conductivity in Nanopores **13**

2.1 Introduction 13

2.2 Theory 15

2.3 Results and Discussion 18

2.3.1 Buffer effect from surface and saturation of conductivity . . . 19

2.3.2 Effect of isoelectric point and ΔpK on conductivity 21

2.3.3 Channel Conductivity Reduction 25

2.4 Conclusion 28

3 Charge Regulation at Semiconductor-Electrolyte Interfaces 31

3.1 Charge regulation at an isolated semiconductor electrolyte interface . 34

3.2 Interaction between Semiconductor Colloidal Particles in Electrolyte Solution 38

4 Charge Regulating Density Functional Theory of Electric Double Layers 49

4.1 Theory 51

4.1.1 Formulation of Interactions 52

4.1.2 Boundary Conditions 53

4.2 Results 57

4.3 Conclusion 62

5 Summary and Conclusions 65

Appendices **66**

A Calculations of energy of interaction between colloidal particles **67**

B Linearization of the surface potential subject to charge regulation **70**

C Charge Density Determined by the Fermi-Dirac Distribution **74**

D Fermi Level at a Semiconductor-Oxide-Electrolyte Interface **76**

E Derivation of boundary conditions for density functional calculation **78**

F Documentation of Python Interface for Running Tramonto **80**

References **83**

List of Figures

2.1 Surface $p\mathrm{H}_s$ vs. bulk reservoir $p\mathrm{H}_b$ for various channel widths. (a) Corresponds to a surface with parameters, $p\mathrm{I} = 4$, and $\Delta p\mathrm{K} = 8$, and (b) corresponds to a surface with parameters $p\mathrm{I} = 8$, and $\Delta p\mathrm{K} = 4$. The dashed line in each figure corresponds to the bulk limit where no buffering is present, that is, $p\mathrm{H}_b = p\mathrm{H}_s$. 17

2.2 Surface $p\mathrm{H}_s$ vs. bulk reservoir $p\mathrm{H}_b$ for various channel widths. (a) Corresponds to a surface with parameters, $p\mathrm{I} = 4$, and $\Delta p\mathrm{K} = 8$, and (b) corresponds to a surface with parameters $p\mathrm{I} = 8$, and $\Delta p\mathrm{K} = 4$. The dashed line in each figure corresponds to the bulk limit where no buffering is present, that is, $p\mathrm{H}_b = p\mathrm{H}_s$. 20

2.3 Plots of channel conductivity vs. $p\mathrm{H}_b$ for various channel widths. These plots illustrate conductivity saturation for parameters, (a) $p\mathrm{I} = 4$, and $\Delta p\mathrm{K} = 8$, and (b) $p\mathrm{I} = 8$, and $\Delta p\mathrm{K} = 4$. 21

2.4 Normalized channel conductivity in a 100 nm channel as a function of $p\mathrm{H}_b$ and $\Delta p\mathrm{K}$. (a) Corresponds to a surface isoelectric point, $p\mathrm{I} = 4$, (b) $p\mathrm{I} = 7$, and (c) $p\mathrm{I} = 10$. 22

2.5 Plots of normalized conductivity vs. $p\mathrm{H}_b$ for various channel widths, and charge regulating surface properties, (a) $p\mathrm{I} = 4$, and $\Delta p\mathrm{K} = 8$, and (b) $p\mathrm{I} = 8$, and $\Delta p\mathrm{K} = 4$. 24

2.6 Plots of normalized conductivities vs. $p\mathrm{H}_b$ for various channel widths, and that demonstrate conduction reduction for parameters (a) $p\mathrm{I} = 4$, and $\Delta p\mathrm{K} = 8$, and (b) $p\mathrm{I} = 8$, and $\Delta p\mathrm{K} = 4$. 26

2.7 Plots of channel conductivities vs. $p\mathrm{H}_b$ for channels of various widths with parameters $p\mathrm{I} = 4$, and $\Delta p\mathrm{K} = 8$. 27

2.8 Plot of conductivity normalized with respect to the channel conductivity at neutral $p\mathrm{H}$, $\gamma_c^N = \gamma_c/\gamma_N$, where γ_N is the conductivity inside the channel at neutral $p\mathrm{H}$, i.e., $\gamma_N \equiv \gamma_c(p\mathrm{H} = 7)$. Two systems are represented one with charge regulation parameters, $p\mathrm{I} = 4$, and $\Delta p\mathrm{K} = 8$, and the second with parameters, $p\mathrm{I} = 4$, and $\Delta p\mathrm{K} = 2$. Solid lines represent γ_c^N with the axis on the left side, while dashed lines represent $p\mathrm{H}_{\mathrm{min}}$ (the $p\mathrm{H}$ of the bulk reservoir where conductivity is minimized) with the axis on the right side. 29

3.1 One dimensional potential distributions in the electrolyte solution (red), oxide layer (black), and the semiconductor (blue) approximated as infinite flat plates. The solid line corresponds to two particles separated by 10 nm, while the dashed line corresponds to the potential distribution of a single particle in isolation. These curves illustrate how the potential distribution inside the semiconductor responds to the presence of an approaching colloid. The particles are covered with $-\mathrm{SiO}^-$ groups with surface density $\Gamma = 8 \times 10^{18}$ m^{-2}. These groups may release or attach a proton according to Eq. (3.1). The parameters for this calculation are: $p\mathrm{H} = 3.5$, the overall electrolyte concentration is 0.925 mM (adjusted by adding symmetric monovalent electrolyte), $p\mathrm{K}_+ = -2$, $p\mathrm{K}_- = 6$, and the particle doping is 10^{24} m^{-3}. The dielectric permitivities were $\varepsilon_{\mathrm{el}} = 78.5$ for the electrolyte, $\varepsilon_{\mathrm{sc}} = 11.7$ for Si, and $\varepsilon_{\mathrm{ox}} = 3.9$ for the 2 nm thick layer of SiO_2 [1, 2]. 35

3.2 Potential distributions plotted as a function of distance z. The semiconductor/oxide interface is at $z = 50$ nm while the oxide/electrolyte interface is at $z = 52$ nm. The various lines depict varying doping concentrations. The inset is a plot of surface potential Ψ_s versus doping N_d. 36

3.3 Potential distributions plotted as a function of distance z. The parameters are the same as those given in Fig. 3.2 but at constant doping of $N_d = 10^{18} cm^{-3}$. The inset is a plot of the surface potential Ψ_s versus Debye length κ^{-1}. 37

3.4 Potential distributions plotted as a function of distance z for different values of ΔpK. The parameters are the same as those given in Fig. 3.2 but at constant doping of $N_d = 10^{18}\ cm^{-3}$. The inset shows surface potential versus ΔpK. 37

3.5 Visualization of system consisting of two particles. Axis symmetry along z with the other spatial coordinate r results in the two particles being spherical in geometry. The separation of the particles is given as h, and the radius of the particles is a. The shaded portions represent the magnitude of the potential Ψ for a particular set of values, darker shades indicate larger values. It can be seen that the smallest values of Ψ are far from the particle surface in the electrolyte, as well as deep in the interior of the semiconductor particles. At this scale the oxide layer is too thin to be easily seen. 39

3.6 Interaction energy versus separation h. The solid line is for two undoped particles, a noticeable reduction in free energy can be seen for the various combinations of doped particle interactions. The inset provides a closer look at the peak of the doped particle interaction energies. 40

3.7 Interaction energy versus separation h. The solid lines are for undoped spherical particles and the dashed lines are for their doped counterparts where $N_d = 10^{18}/cm^3$. 41

3.8 Potential distributions of a one dimensional semiconductor-oxide-electrolyte system demonstrating the difference between the approximation described in Eq. (3.6). The dashed lines were calculated using Boltzmann statistics while the full lines were calculated by numerically evaluating the Fermi integral in Eq. (3.3). 42

3.9 Interaction between colloids. Interaction energy between undoped (blue particles, full line) and doped (red particles, dashed line) semiconductor colloids. As the particles approach the charge density in the doped particles redistribute which is illustrated by the gradual color change. The Hamaker constant used to generate this plots is $A_H = 5.4 \times 10^{-20}$ J, and the particle radius is a = 100 nm. The rest of the parameters are the same as in Figure 3.1. The inset shows the difference between the two energy curves. 43

3.10 Differences in stability due to doping. (a) Stability of undoped (dashed) and doped colloids (solid) vs. semiconductor doping concentration. The stabilities are useful for calculating time to coagulation. The inset shows relative stability $W_{\text{undoped}}/W_{\text{doped}}$ vs. doping. The relative stability is useful for calculating relative times to coagulation for undoped vs. doped particles. (b) Stability of undoped (dashed) and doped colloids (solid) vs. ionic concentration of the electrolyte. The relative stability $W_{\text{undoped}}/W_{\text{doped}}$ vs ionic concentration of the electrolyte is given in the inset. The rest of the parameters are the same as in Figs. 3.1 and 3.9 44

4.1 Normalized density distributions using DFT (solid) and Poisson-Boltzmann (dashed) with the same surface charge density. While these two systems have the same surface charge density, the contact value $z = 0$ for the normalized densities are quite different with DFT giving a much larger value for all species. 55

4.2 Illustration of the effect of structure on the density distribution using DFT subtracted from the density distribution using Poisson-Boltzmann (blue). The peaks (red dots) of the effect of structure are fitted with an exponential (yellow dashed) to illustrate the structure decay length. 55

4.3 Comparison between DFT and Molecular Dynamics results. It can be seen that the density profiles for a hard-sphere solvent with diameter d_s and Lennard-Jones interactions with (a) $\epsilon = 0.0\ k_BT$, (b) $\epsilon = 0.5\ k_BT$, and (c) $\epsilon = 1.0\ k_BT$ are all very close to each other demonstrating that DFT and Molecular Dynamics will give nearly the same results for the domain of interest in this dissertation. The DFT results shown here were all generated with the choice of hard sphere diameters $d_{\text{HS}} = d_{ij}$. 57

4.4 Surface charge of an EDL as a function of the solvent molecular diameter. The different curves are for different values of the LJ parameter ϵ_{LJ}. Markers on each line represent points where simulations successfully ran, there are several locations in both plots where we were unable to obtain results, either due to numerical instabilities, or due to prohibitively long compute times. 58

4.5 Solution structure in terms of density distribution functions in the vicinity of the charged surface. Molecular diameter of solvent is $d_s = 0.0288$ Å Although calculated using DFT, this represents the "primitive" model limit where d_s is close to zero. (a) Hard boundary conditions using Eq. (4.7). There is no discernable structure for the neutral solvent while the positive and negative ions follow distributions identical to the modified Poisson–Boltzmann limit. (b) Soft boundary conditions using Eq. (4.8). Notice that the surface charge obtained using the soft boundary conditions is higher than using the hard boundary conditions. 60

4.6 Solution structure in terms of density distribution functions in the vicinity of the charged surface. Solid lines correspond to $\epsilon_{\text{LJ}} = 0.0\ k_BT$, dashed lines correspond to $\epsilon_{\text{LJ}} = 0.4\ k_BT$ Molecular diameter of solvent is $d_s = 2.3$ Å for a dimensionless density of $\rho d_s^3 = 0.41$ which corresponds to a supercritical fluid. (a) Hard boundary conditions using Eq. (4.7). (b) Soft boundary conditions using Eq. (4.8). Notice that the surface charge obtained using the soft boundary conditions is higher than using the hard boundary conditions. 62

4.7 Plots of solution structure in terms of density distribution functions in the vicinity of the charged surface. Solid lines correspond to $\epsilon_{\text{LJ}} = 0.0\ k_BT$, dashed lines correspond to $\epsilon_{\text{LJ}} = 0.4\ k_BT$ Molecular diameter of solvent is $d_s = 2.88$ Å for a dimensionless density $\rho d_s^3 = 0.8$. (a) Hard boundary conditions using Eq. (4.7). (b) Soft boundary conditions using Eq. (4.8). Notice that the surface charge obtained using the soft boundary conditions is higher than using the hard boundary conditions. 63

B.1 Surface potential for undoped and doped particles as a function of distance. Both numerical and analytical [see Eq. (B.13)] results are shown for comparison. 73

D.1 Fermi level μ vs the parameter χ. 77

List of Tables

2.1 Diffusion Constants for Ions 18

Glossary

δ	For chapter one, δ is the thickness of Stern layer. Units of $[m]$. For all other chapters $\delta \equiv 2\sqrt{K_-/K_+}$ and is unitless.
ε_0	Permittivity of free space. Units of $[F/m]$.
ε_{el}	Relative permittivity of the electrolyte. Unitless.
ε_{ox}	Relative permittivity of the oxide. Unitless.
ε_r	Relative permittivity. Unitless.
ε_{sc}	Relative permittivity of the semiconductor. Unitless.
Γ	Concentration of ionizable groups at the surface. Units of $[m^{-2}]$.
γ^*	Normalized conductivity. Unitless.
γ_c	Conductivity of the solution in confinement. Units of $[S/m]$.
γ_b	Conductivity of the bulk solution. Units of $[S/m]$.
η	Viscosity of solvent. Units of $[Pa \cdot s]$.
Λ	Thermal de Broglie wavelength. Units of $[m]$.
σ_s	Surface charge density. Units of $[C/m^2]$.

ρ	Total charge density. Units of $[C/m^3]$.
Ψ	Electrostatic potential. Units of $[V]$.
$\widetilde{\Psi}$	Scaled electrostatic potential so that, $\widetilde{\Psi} = e\Psi/k_BT$. Unitless.
Ψ_N	Nernst potential. Units of $[V]$.
Ψ_s	Electrostatic potential at the dielectric-electrolyte interface. Units of $[V]$.
Ψ_q	Electrostatic potential at the semiconductor-oxide interface. Units of $[V]$.
ζ	Zeta potential. For the purpose of this paper we consider $\zeta = \Psi_s$.
Ω	Grand free energy functional
a	Particle radius. Units of $[m]$.
A_H	Hamaker constant. Units of $[J]$.
D_i	Ionic diffusion coefficient of component i. Units of $[m^2/s]$.
d_s	Diameter of solvent. Units of $[m]$.
e	Fundamental unit of charge. $1.602176565\times10^{-19}C$
EDL	Electrostatic double layer
h	In the discussion about the Ornstein–Zernike equation h refers to Plank's constant and has a value of $6.62606957 \times 10^{-34}Js$. Everywhere else h refers to the distance between two parallel infinite flat plates. Units of $[m]$.
$\hbar$	Reduced Planck's constant. Has value of $1.054571 \times 10^{-34}Js$.

K_- and K_+	Dissociation constants that determine chemical equilibrium for an interface.
k_B	Boltzmann's constant. $1.3806488 \times 10^{-23} J/K$.
L_{ox}	Width of oxide layer. Units of $[m]$.
LJ	Lennard–Jones
$\mathbf{n}$	Unit vector normal to the surface and pointing into the electrolyte.
m^*	Effective mass of electron in semiconductor region.
OZ	Ornstein–Zernike
PB	Poisson–Boltzmann equation
$p\text{H}_b$	pH of the bulk solution far from the surface.
$p\text{H}_s$	pH at the electrolyte-solid surface.
PDI	Potential determining ion. For this dissertation the PDI is always H_3O^+.
n_i^0	Bulk number concentration of ion i. Units of $[m^{-3}]$.
T	Temperature. Always 298.15 K for this document.
z	Spatial coordinate. Units of $[m]$.
z_i	Charge number of ion i. Unitless.

Chapter 1

Introduction

Electrostatic fields often occur and determine the physical and chemical behavior of solutions at the nanometer length scale in the vicinity of interfaces. The origin of the electrostatic potentials lies in the interaction of an interface with an adjacent polar liquid (usually water). This interaction may include dissociation of surface ionic groups or adsorption of ions from the bulk or both, and is often governed by maintaining chemical equilibria between the surface groups and the adjacent electrolyte.

The presence of adsorbed ions at solid-electrolyte interfaces results in the formation of an electric double-layer (EDL) [3]. The electric double layer is comprised of the adsorbed ions at the interface, and a diffuse layer of coions, and counter ions in the electrolyte that are constantly in motion. Though the ions in the electrolyte are constantly in motion, they have a well defined distribution away from the interface that is governed by a competition between their attraction or repulsion from the interface, and thermal fluctuations. At a distance far away from the interface the distribution of ions tends towards their bulk values. In this dissertation, we study the phenomenon of surface charge regulation in the context of fluidic nanoscale systems

and obtain an improved fundamental understanding of the electrostatic properties of solid-electrolyte interfaces. By extending upon charge regulating theory, we make predictions about the *p*H dependence of fluidic nanochannels, stability of doped semiconductor colloids, and the effect of solvent structure on charged interfaces using density functional theory of fluids.

1.1 Background and Literature Overview

The development of theories regarding charged surfaces in contact with electrolytes has a rich history involving well over a century of activity. The earliest theories were developed in 1853 by Helmholtz who coined the term 'double layer' which he described as a charged electrode in an electrolyte solution with a counter balanced charged within the electrolyte resulting in charge neutrality for the entire system [4]. From this realization, Helmholtz was able to demonstrate that the electrostatic double layer stores charge, and therefore behaves as a capacitor.

1.1.1 Continuum Approach – The Poisson Boltzmann Equation

The first theoretical description of the EDL was developed independently by Gouy [5] and Chapman [6]. The Gouy–Chapman model of the electrostatic double layer is described as a distribution of ions near the interface using Boltzmann statistics. In this model, ions in the electrolyte are described as point charges, the solvent is described as a structureless medium through the dielectric constant, and the charge of the interface is averaged to provide a uniform surface charge density [7]. These assumptions are appropriate when length-scales are large enough that the solvent can be treated as a continuum and ion concentrations are low enough that ion-

ion correlations are small [8–10]. The Poisson–Boltzmann equation is based on the Gouy–Chapman model and is used to calculate potential distributions. The equation is derived simply by combining the Poisson equation

$$\nabla^2\Psi = -\frac{\rho}{\varepsilon_0\varepsilon_r}, \tag{1.1}$$

and the charge density ρ subject to Boltzmann statistics

$$\rho = e\sum_i z_i n_i^0 \exp\left(\frac{-z_i e\Psi}{k_B T}\right), \tag{1.2}$$

so that we arrive at the Poisson–Boltzmann equation [3, 11]

$$\nabla^2\Psi = -\frac{e}{\varepsilon_0\varepsilon_r}\sum_i z_i n_i^0 \exp\left(\frac{-z_i e\Psi}{k_B T}\right), \tag{1.3}$$

where Ψ is the electrostatic potential, ε_0 is the permittivity of free space, ε_r is the relative permittivity of the fluid, e is the fundamental unit of charge, z_i is the charge number of the i^{th} ion, n_i^0 is the bulk number density of the i^{th} ion, and $k_B T$ is the thermal energy of the system.

For the purpose of this dissertation we will only consider symmetric monovalent electrolytes, and for that cause the PB equation simplifies to

$$\nabla^2\Psi = \frac{k_B T}{e}\kappa^2 \sinh\left(\frac{e\Psi}{k_B T}\right), \tag{1.4}$$

where κ is the inverse Debye screening length, and is defined as

$$\kappa^{-1} = \sqrt{\frac{\varepsilon_r\varepsilon_0 k_B T}{2N_A e^2 n^0}}, \tag{1.5}$$

where N_A is Avogadro's constant.

Since the Poisson–Boltzmann equation Eq. (1.3) is a 2nd order differential equation, it is necessary to have two boundary conditions to obtain a unique solution. Typically these boundary conditions are taken at interfaces, infinitely far from the interface, or at a midpoint region for systems that exhibit symmetry. When using

the boundary condition at the interface it is common to use Direchlet or Neumann boundary conditions which correspond to constant potential, and constant surface charge density respectively. For a constant potential boundary condition we use

$$\Psi_s = \Psi(0). \tag{1.6}$$

and for a constant surface charge density boundary condition we use

$$\sigma_s = -\varepsilon_r \varepsilon_0 \nabla \Psi. \tag{1.7}$$

Solutions to Eq. (1.3) provide the potential distribution of a diffuse double layer where the density of ions decays roughly exponentially towards bulk density away from the interface.

Since the Gouy–Chapman model assumes ions have no size, it tends to overestimate the concentration of ions near the interface. This pitfall becomes readily apparent with highly charged surfaces where solutions to the PB equation demand that the concentration of ions be larger than what is sterically allowed. Several modifications to the Gouy-Chapman model have been proposed in order to account for ion size at the interface. The first modification was proposed by Stern which involves combining the Helmholtz and Gouy–Chapman models and introducing the so-called Stern layer [12] which is an impenetrable layer of ions adsorbed to the surface combined with an adjacent diffuse Gouy–Chapman layer. The Stern layer is constructed so that the concentration of ions at the surface does not exceed the available volume [12]. More recent improvements to the Gouy–Chapman model are based on modifying the Poisson–Boltzmann equation in such a way as to include finite size effects of ions [13–17]. While these modifications to the PB equation have provided useful extensions to the original Gouy–Chapman model, they do not account for the interaction between solvent and ions which leads to omission of important physical effects.

It was recognized that the above theories could be applied to the interaction

of two approaching surfaces both having EDLs. This gave rise to the celebrated DLVO theory developed in 1941 by Derjaguin and Landau [18] and independently by Verwey and Overbeek in 1948 [3]. In it's simplest form, the DLVO theory makes use of the Gouy–Chapman model to determine the repulsive interaction due to the presence of two overlapping double layers combined with the attractive van der Waals interaction [19]. The competitive combination of these two interactions provides an explanation for the stability of colloidal systems.

1.1.2 Introduction to Charge Regulation

Calculation of the potential distribution using the PB equation is straightforward when using Dirichlet or Neumann boundary conditions, corresponding to constant surface potential, and constant surface-charge density respectively [3]. However, the physically relevant boundary condition is given by the chemical equilibrium between free and bound ions at the surface. This is particularly important if one needs a better quantitative description of the potential as a function of various environmental parameters, particularly at the nanoscale. Such situations occur in phenomena involving colloid stability, nanofabrication and assembly, and transport phenomena in nanochannels.

Charge regulation boundary conditions were first formulated by Ninham and Parsegian [20]. Later Chan, et al. generalized the approach to include dissimilar surfaces [21]. An exact solution to the PB equation using charge regulating boundary conditions was derived by Behrens and Borkovec [22] and a variety of other charge regulation models have been developed that account for the Stern layer, ion adsorption [23], while others make use of various approximations to the chemical equilibria [24, 25].

The charge regulation model we use assumes that the interface can be described

as an amphoteric surface "A" that participates in two chemical equilibria,

$$\begin{aligned} \mathrm{AH_2^+ + H_2O} &\rightleftharpoons \mathrm{AH + H_3O^+} \qquad (K_+) \\ \mathrm{AH + H_2O} &\rightleftharpoons \mathrm{A^- + H_3O^+} \qquad (K_-) \end{aligned} \tag{1.8}$$

where K_+ and K_- are the dissociation constants. According to these two chemical equilibria, the amphoteric surface can acquire a negative, positive or neutral charge. The boundary conditions are then expressed in terms of the surface charge density as a function of surface potential $\sigma(\Psi_s)$ [20, 21]

$$\sigma(\Psi_s) = e\Gamma \frac{[\mathrm{AH_2^+}] - [\mathrm{A^-}]}{[\mathrm{AH}] + [\mathrm{AH_2^+}] + [\mathrm{A^-}]}, \tag{1.9}$$

then using statistical mechanics we can substitute concentrations with electrostatic potentials [20, 21]

$$\sigma(\Psi_s) = e\Gamma \frac{\delta \sinh[e(\Psi_N - \Psi_s)/k_B T]}{1 + \delta \cosh[e(\Psi_N - \Psi_s)/k_B T]}, \tag{1.10}$$

where $\delta \equiv 2\sqrt{K_-/K_+}$, Γ is the surface concentration of ionizable groups at the surface, and Ψ_s is the potential at the surface of the nanochannel. The Nernst potential [21] is

$$\Psi_N = \ln(10) \frac{k_B T}{e} \left(p\mathrm{I} - p\mathrm{H}_b\right), \tag{1.11}$$

the isoelectric point of the surface is expressed by

$$p\mathrm{I} = \frac{p\mathrm{K}_+ + p\mathrm{K}_-}{2}, \tag{1.12}$$

and for mathematical convenience we use a quantity $\Delta p\mathrm{K}$ which is defined as

$$\Delta p\mathrm{K} = p\mathrm{K}_- - p\mathrm{K}_+, \tag{1.13}$$

where $p\mathrm{K}_\pm = -\log_{10}(K_\pm)$.

By satisfying the boundary conditions given in Eq. (1.9) chemical equilibria will be satisfied at the interface. This allows us to express our boundary conditions in terms of pH, and surface chemistry parameters pI, and ΔpK which are physically justified.

1.1.3 Statistical Mechanical Models Based on the Ornstein–Zernike Equation

A more rigorous approach for theoretical analysis of the EDL is based on finding solutions to integral equations using statistical mechanics [26–31]. Statistical mechanical models offer a vastly superior treatment of EDLs since they explicitly account for the ionic size and interaction not only at the interface, but everywhere in the bulk solution. These improved models include the BBGKY hierarchy which attempt to extend the Boltzmann equation to higher densities by approximating pair distribution functions as singlet distribution functions, unfortunately this method produces terms that diverge for many quantities of interest [32]. A substantial portion of the recent statistical mechanical analysis of electrolytes and EDL is based on solving the Ornstein–Zernike (OZ) equation which for multicomponent solutions has the form [32–35]

$$h_{ij}(\mathbf{r}_1, \mathbf{r}_2) = c_{ij}(\mathbf{r}_1, \mathbf{r}_2) + \sum_k \rho_k \int d\mathbf{r}_3 c_{jk} c_{ij}(\mathbf{r}_1, \mathbf{r}_2) h_{ij}(\mathbf{r}_1, \mathbf{r}_2), \tag{1.14}$$

where h_{ij} and c_{ij} are the total and direct correlation functions between particles of species i and j, ρ_k is the number density of species k and $\mathbf{r}_1$, $\mathbf{r}_2$, and $\mathbf{r}_3$ are position vectors. Eq. (1.14) has to be accompanied by a closure relation [32, 33], which provides an expression for the direct correlation function $c_{ij}(\mathbf{r}_1, \mathbf{r}_2)$ or $h_{ij}(\mathbf{r}_1, \mathbf{r}_2)$. While the OZ equation is derived in a rigorous procedure, the closure is based on physical assumptions, and in essence is an approximation. This may lead to anomalies such as different results for the pressure when obtained directly from the pressure equation or by integrating the compressibility equation [32, 33]. There are ways to force the two methods to give the same result but they are based on mathematical interpolation [36] instead of a true physical self-consistency. In additions to that, in order to simplify the problem, the OZ approach is often applied only to the ionic species, while the solvent is considered as being a structureless medium. This so-

called "primitive" model, has been widely used for decades [34,35,37,38], and is still used today [39, 40]. A more realistic but complicated alternative is the "civilized" model (a term suggested by R. H. Stokes [41]), which explicitly accounts for the molecular structure of the solvent [42–47]. The latter works employ a mean spherical approximation for the closure relationship, which allows for a relatively simple solution at the expense of being approximate.

Recently charge regulation has been coupled to Ornstein–Zernike using the "primitive" model [39]. In this model only ions are considered, and the role of the solvent structure is ignored.

1.1.4 Density Functional Theory of Electric Double Layers

An alternative approach to the OZ equation is the classical Density Functional Theory (DFT) [40, 48–68]. DFT is the method of choice because it is particularly convenient to model fluids in an external field, which is what an EDL represents. DFT does not require a closure relationship, but derives the solution structure through minimization of the grand thermodynamic potential with respect to the density of all components in the system. The free energy functional is known exactly for hard rods in one dimension [49–51, 68]. For other systems the functional is not known exactly, but very good approximations are available. Hence, the final results depend on the accuracy of the grand thermodynamic or free energy functionals.

Fortunately, previous work [40,48–68] has provided guidelines on how to construct and work with such functionals. For example, the grand potential for flat EDLs composed by a system of interacting ions and molecules [48, 67] is given by

$$\begin{aligned}\Omega[\{\rho_i\}] = F_{\mathrm{id}}\left[\{\rho_i\}\right] + F_{\mathrm{HS}}^{\mathrm{ex}}\left[\left\{\overline{\rho_i^{\mathrm{HS}}}\right\}\right] + F_{\mathrm{long}}^{\mathrm{ex}}\left[\left\{\overline{\rho_i^{\mathrm{long}}}\right\}\right] \\ + \sum_{i=1,N}\int d\mathbf{r}\rho_i(\mathbf{r})\left[V_i^{\mathrm{ext}}(\mathbf{r}) - \mu_i\right], \end{aligned} \tag{1.15}$$

where the ideal contribution to the free energy is given as

$$F_{\mathrm{id}}\left[\{\rho_i\}\right] = k_B T \sum_{i=1,N} \int d\mathbf{r} \rho_i(\mathbf{r}) \left\{ \ln\left[\Lambda_i^3 \rho_i(\mathbf{r})\right] - 1 \right\}. \tag{1.16}$$

$F_{\mathrm{HS}}^{\mathrm{ex}}\left[\left\{\overline{\rho_i^{\mathrm{HS}}}\right\}\right]$ is the Helmholtz excess free energy functional for a hard sphere mixture, $F_{\mathrm{long}}^{\mathrm{ex}}\left[\left\{\overline{\rho_i^{\mathrm{long}}}\right\}\right]$ is the long range contribution (usually attractive), h is Planck's constant, m_i is the mass of the molecule "i", $\Lambda_i = \sqrt{h^2/(2\pi m_i k_B T)}$, $\rho_i(\mathbf{r})$ is the variation of the local density of component i with the distance from the charged interface, V_i^{ext} is the electrostatic potential, μ_i is the chemical potential, and Φ_{ij} are the interaction energies (including the excluded volume, i.e. "hard sphere") between species i and j. Other possible contributions are electrostatic (Coulombic), and van der Waals attraction (e.g., LJ). The interaction energy is assumed to be pair-wise additive. The special case of applying DFT to electrolytes in hard-sphere solvent was studied by Frink and van Swol. For a solution that exhibits hard-sphere, electrostatic, LJ and anisotropic interactions (dipole-dipole, ion-dipole) the interaction energy will have the following contributions,

Hard sphere, LJ and ion-ion interactions are given as

$$\Phi_{LJ}\left(r_{ij}\right) = \begin{cases} 4\epsilon_{ij}\left[\left(\frac{d_{ij}}{r_{ij}}\right)^{12} - \left(\frac{d_{ij}}{r_{ij}}\right)^{6}\right], & r_{ij} > d_{ij} \\ r_{\min}, & r_{ij} \leq d_{ij}, \end{cases} \tag{1.17}$$

and hard sphere LJ and ion-wall interactions are given as

$$\Phi_{LJ}\left(r_{ij}\right) = \begin{cases} \frac{2\pi}{3}\epsilon_{ij}\left[\frac{2}{15}\left(\frac{d_{ij}}{r_{ij}}\right)^{9} - \left(\frac{d_{ij}}{r_{ij}}\right)^{3}\right], & r_{ij} > d_{ij} \\ r_{\min}, & r_{ij} \leq d_{ij}, \end{cases} \tag{1.18}$$

where d_{ij} is the center to center distance between species i and j, d_i is the center to wall distance and ε_{ij} is the respective LJ energy parameter. The powers in the LJ term in Eq. (1.18) are (9-3) instead of (6-12) [see Eq. (1.17)] because they are integrated over the bulk of the wall (see for example Problem 7.1 in Ref. [69]).

While the "civilized" model accounts for the explicit structure of the solvent, for low electrolyte concentrations the electrostatic interactions between the ions or the ions and the wall, can be reasonably approximated by the macroscopic effect of the solvent as defined by the relative dielectric permittivity ε_r [41, 43, 70]. This means that all Coulombic and dipole terms in the above equations have to be divided by ε_r. A particularly useful discussion how to implement the dielectric effect in all electrostatic interactions is given in Refs. [41,43]. Different thermodynamic quantities of interest can be obtained through functional differentiation of Ω or $F_{\rm HS}^{\rm ex}\left[\left\{\overline{\rho_i^{\rm HS}}\right\}\right]$ [see Eq. (1.15)]. In fact functional differentiation provides formally exact results [51]. Hence, the accuracy of the final results depends on how good the approximation is for the functional.

The density distribution functions for each component $\rho_i(z)$ (ionic or solvent) are determined for the minimization condition [49–51]

$$\frac{\delta\Omega\left[\rho_1(z),\rho_2(z),...,\rho_N(z)\right]}{\delta\rho_i(z)}=0. \tag{1.19}$$

Integrating over the charged species densities in the EDL will give the total amount of excess charge in the bulk, which is equal to the charge at the interface thus maintaining overall charge neutrality. Hence Eq. (1.19) gives the local structure of the solution from which one can deduce the surface charge and potential if required.

1.2 Motivation

Charged interfaces that develop in electrolyte solutions are of fundamental interest to many science and engineering problems and a better understanding of these systems presents opportunities for obtaining physical insights and novel applications.

For example, experimental results on the conductivity of nanochannels have demonstrated interesting new phenomena including significant deviations of conduc-

tivity from bulk values [71, 72], ion-current rectification [73, 74], saturation of conductivity at low concentrations [72], and have related *p*H to ionic conductance [75].

The interface between semiconductor and electrolyte solution is also of fundamental interest and has not been studied in great detail. It also presents opportunities for new and exciting applications. Recent experiments [76, 77] have demonstrated that the charge density inside a doped semiconductor in the vicinity of a semiconductor-electrolyte interface will shift in response to changes in the electrostatic potential in the electrolyte phase. This effect has been exploited to perform force measurements and is utilized in a significant number of sensing applications that make use of nanoscale semiconductors [78–85]. Semiconductor colloids have potential for fabricating new smart and enabling materials [86] with electronic and optoelectronic applications [87–91]. Based on all these studies, we believe that a theoretical framework for the analysis of semiconductor-electrolyte interfaces is necessary and will provide many interesting fundamental advancements for this class of emerging materials.

1.3 Brief outline of Dissertation

Chapter 1 provides an introduction and motivation for theories of the EDL, including discussions of models based on solutions to the Poisson equation that have no finite size effects, modified Poisson equations that attempt to account for finite size of ions, OZ which can account for finite sizes of ions and solvent, and DFT which can account for finite size of ions and solvent in a physically self-consistent manner.

In Chapter 2 the phenomenon of charge regulation is presented in a rigorous manner. Solutions to the Poisson–Boltzmann equation using charge regulation are analyzed in the context of conductivity of fluidic nanochannels, and an in-depth discussion is provided on how *p*H affects the conductivity of nanochannels. The

*p*H of the bulk solution and the isoelectric point of the interior of the nanochannel are demonstrated to be key parameters, and several counter-intuitive results are presented including conductivity reduction relative to bulk conductivity at *p*H near the isoelectric point of the interface. Much of the work in this chapter has been published in [J. Coll. Interf. Sci. 416 (2014) p. 105–111] [92].

In Chapter 3 the coupling of the semiconductor-electrolyte interface is explored using charge regulation. The effect of charge regulation on doped semiconductor-electrolyte interfaces is demonstrated to have a significant impact on the stability of doped semiconductor colloids using DLVO theory. Other effects at semiconductor-electrolyte interfaces are explored including the effect of doping on the surface potential, salt concentration, and surface chemistry. A discussion of the importance of using Fermi-Dirac statistics inside the semiconductor domain for high doping concentrations is also presented, and results are compared to those obtained using the more approximate Maxwell-Boltzmann statistics. Much of the work in this chapter has been published in [Phys. Rev. Lett. 113 (2014) 158302] [93], and "Charge Regulation at Semiconductor–Electrolyte Interfaces" (Accepted in Journal of Colloid and Interface Science, awaiting publication).

Chapter 4 develops a theory using DFT and charge regulation that accounts for finite size effects and attractive interactions between both solvent and ion species. The effect of solvent size is shown to have a significant impact on the surface charge.

Chapter 5 presents a brief summary and conclusion to the dissertation.

Chapter 2

Effects of Charge Regulation on Conductivity in Nanopores

2.1 Introduction

The precise electrostatic potential distribution is very important for determining the electrokinetic transport in fluidic channels. This is especially valid for small nanochannels where the electric double layers formed at the walls are comparable to the channel width. It can be expected that due to the large surface to volume ratio in such systems, they will exhibit properties that are not detectable in larger channels, capillaries and pores. In this chapter, we present a detailed theoretical analysis of the current transport in fluidic nanochannels. It is based on solving the continuous Poisson-Boltzmann equation with charge regulation boundary conditions that account for the surface-aqueous solution chemical equilibria. The focus is on studying the effect of the pH on the current transport. The pH is varied by adding either HCl or KOH. The analysis predicts non-monotonous and sometimes counterintuitive dependence of the conductivity on the pH. The channel conductivity exhibits

practically no change over a range of pH values due to a buffering exerted by the chemical groups at the walls. An unexpected drop of the conductivity is observed around the wall isoelectric point and also in the vicinity of $p\mathrm{H} = 7$ even though the concentration of ions in the channel increases relative to the concentration of ions in the bulk. These observations are explained in the framework of charge regulation theory.

The mathematical derivation of the electrostatic potential using a continuum approximation based on the Poisson–Boltzmann (PB) equation is simple when using Dirichlet or Neumann boundary conditions, corresponding to constant surface potential, and constant surface-charge density respectively [3]. However, the physically relevant boundary condition is given by the thermodynamic equilibrium between free and bound ions at the surface. This is particularly important if one needs a better quantitative description of the potential as a function of various environmental parameters particularly at the nanoscale. Such situations occur in phenomena involving colloid stability, nanofabrication and assembly, and transport phenomena in nanochannels.

Charge regulation boundary conditions for solving the electrostatic problem were first formulated by Ninham and Parsegian [20]. Later Chan, et al. [21] generalized the approach to include dissimilar surfaces. A closed-form analytical solution to the PB equation using charge regulating boundary conditions was derived by Behrens and Borkovec [22]. A variety of other charge regulation models have been developed that account for the Stern layer, ion adsorption [23], and they make use of various approximations to the chemical equilibria [24, 25].

The surface charge or potential of a nanochannel has a strong influence on ionic conductivity. This is due to redistributing the counter ions and coions in the electric double-layer which for very small channels occupies most of the volume. We address the effect of the isoelectric point, pH, and surface-bulk chemical equilibria

using a 2-pK [see Eq. (1.13)] charge regulation model [21]. This model has been demonstrated to provide an excellent description of the ionization process of water-solid interfaces [94]. Using this model we calculate the conductivity of ions in a nanochannel. We find that the conductivity can increase, or decrease compared to bulk conductivity depending on the chemical equilibria, and double-layer overlap. Our analysis considers the case of infinite parallel flat plate geometries. Other geometries such as cylindrical are not considered, since the results will be qualitatively similar.

2.2 Theory

The ionic conductivity γ_b of a bulk electrolyte at low concentrations ($<$ 1mM) is determined by [71]

$$\gamma_b = \frac{e^2}{k_B T} \sum_i z_i^2 n_i^0 D_i, \tag{2.1}$$

where e is the fundamental unit of charge, n_i^0 is the bulk number concentration of ion i, $k_B T$ is the thermal energy, D_i are the ionic diffusion coefficients, and z_i are the charge numbers. For low concentrations the diffusion coefficients of the ions are considered to be constant.

In a nanochannel Eq. (2.1) needs to be modified to reflect the effect of the electric double layer near the surfaces of the nanochannel which results from spatially varying ion distributions. The conductivity of the nanochannel of width h is given by γ_c, which includes both surface and electro–osmotic effects becomes [71]

$$\gamma_c = \frac{1}{h}\int_{-h/2}^{h/2} \mathrm{d}z \left[\frac{e^2}{k_B T} \left\{ \sum_i z_i^2 n_i^0 D_i \exp\left[\frac{-z_i e \Psi(z)}{k_B T} \right] \right\} - \frac{\rho(z)\varepsilon_r \varepsilon_0 e[\zeta - \Psi(z)]}{\eta k_B T} \right], \tag{2.2}$$

where z is the spatial coordinate, ε_r is the relative permittivity of the solution, ε_0 is the permittivity of free space, η is the viscosity of the solvent, and $\Psi(z)$ is the potential distribution due to the electric double layer, ρ is the bulk charge density, and ζ is the so-called zeta potential [71,95]. For this study we consider ζ to be equal to the surface potential Ψ_s. Here and below we consider the position $z = 0$ to be located at the center of the system as seen in Fig. 2.1. The second term in the integrand takes into account the convective current due to electroosmotic flow.

In order to calculate the spatially varying potential $\Psi(z)$ we use of the PB equation for a monovalent symmetric electrolyte Eq. (1.3), shown again for convenience

$$\nabla^2 \Psi = \frac{k_B T}{e} \kappa^2 \sinh\left(\frac{e\Psi}{k_B T} \right). \tag{2.3}$$

Since the PB equation is only accurate when ions do not crowd the interface we only consider solutions where the bulk ionic concentration is less than 1 mM and where the counter-ion concentration is less than 0.1 M at the interface.

Two boundary conditions are required to solve the PB equation. The modeled symmetric channel consists of two parallel flat surfaces of identical composition. This is equivalent to setting $\nabla\Psi = 0$ at the center of the system for our first boundary condition.

We are interested in the conductivity dependence on bulk pH when the PDIs are H_3O^+. The charge regulation model is the most appropriate for studying this case. Charge regulation takes place when the surface charge at an interface is controlled by chemical equilibria for adsorption and desorption of potential determining ions.

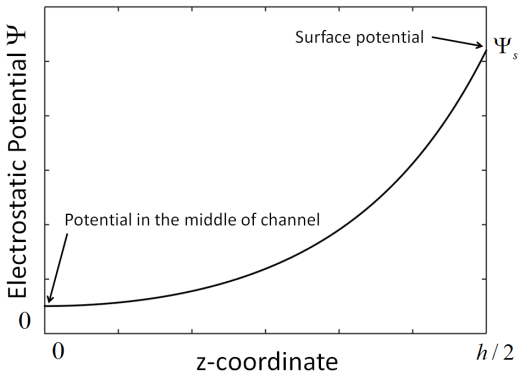

Fig. 2.1: Surface $p\mathrm{H}_s$ vs. bulk reservoir $p\mathrm{H}_b$ for various channel widths. (a) Corresponds to a surface with parameters, $p\mathrm{I} = 4$, and $\Delta p\mathrm{K} = 8$, and (b) corresponds to a surface with parameters $p\mathrm{I} = 8$, and $\Delta p\mathrm{K} = 4$. The dashed line in each figure corresponds to the bulk limit where no buffering is present, that is, $p\mathrm{H}_b = p\mathrm{H}_s$.

For the second boundary condition we use $\Psi(h/2) = \Psi_s$, where Ψ_s is the surface potential. The value of Ψ_s is not known a priori for a given set of charge regulating boundary conditions, but its value is found self-consistently. A guess for Ψ_s is made and used to solve the PB equation to recover $\sigma(\Psi_s)$ and iterated on Eq. (1.9) using a root finding algorithm such as the bisection method in order to satisfy charge regulation. Solutions of the PB equation yield complete information of the ion distributions that we use to compute ionic conductivities for these systems using Eq. (2.2).

The charge regulation model we use assumes that the interface can be described as an amphoteric surface "A" that participates in the two chemical equilibria described in Eq. (1.8) According to these two chemical equilibria, the amphoteric surface can acquire a negative, positive or neutral charge. The boundary conditions are then expressed in terms of the surface charge density as a function of surface potential using Eq. (1.9) [20, 21],

2.3 Results and Discussion

In this study we calculate conductivities of electrolytes in nanochannels with surface charge regulating parameters pI, ΔpK, and Γ. Varying these parameters allows us to illustrate their effect on surface phenomena within the range of experimentally determined values for a number of materials used to construct nanochannels. Example materials include, SiO_2 (pI $\approx$ 2, ΔpK $\approx$ 8, $\Gamma \approx 5$ sites/nm^2), Al_2O_3 (pI $\approx$ 8, ΔpK $\approx$ 4, $\Gamma \approx 8$ sites/nm^2) and Ta_2O_5 (pI $\approx$ 3, ΔpK $\approx$ 2, $\Gamma \approx 10$ sites/nm^2) [96]. For this paper, all results are generated with $\Gamma \approx 8$ sites/nm^2 [96]. We choose this value because it is physically sensible and representative, it reduces our parameter space, and because we do not expect our results to differ qualitatively for different values of Γ.

Bulk pH is controlled by adding either HCl or KOH, and we do not add any background electrolyte, therefore the total ionic strength and hence the Debye length κ^{-1} is dependent on pH. The Debye screening parameter κ is defined as [95]

$$\kappa^2 = \frac{e^2}{\varepsilon_r \varepsilon_0 k_B T} \sum_i z_i^2 n_i^0. \tag{2.4}$$

The diffusion constants necessary to calculate the ionic conductivities are given in Table 2.1. The electrolyte is composed of water with a dissociation constant $p\mathrm{K_w} = 14$ at a temperature of 298.15 K.

Table 2.1: Diffusion Constants for Ions

Ionic species	Diffusion Constant (m^2/s)	Ref.
H^+	9.305×10^{-9}	[97]
K^+	1.957×10^{-9}	[98]
OH^-	5.273×10^{-9}	[98]
Cl^-	2.032×10^{-9}	[98]

2.3.1 Buffer effect from surface and saturation of conductivity

Consider a bulk reservoir in fluidic contact with a nanochannel. Due to chemical interactions with surface groups the pH at the surface of the nanochannel will be different from the pH of the bulk reservoir. We denote the pH of the bulk reservoir as $p\mathrm{H}_b$, and the pH at the surface of the nanochannel as $p\mathrm{H}_s$. The difference in pH between the bulk, and surface is a result of pH buffering [96]. Buffering takes place because the surface of the channel acts as a weak acid or base and can accept, or donate H_3O^+ ions to the solution inside the channel. Fig. 2.2 illustrates the degree of buffering for two different charge regulating surfaces with various channel widths. In Fig. 2.2(a) the charge regulating surface properties are, $p\mathrm{I} = 4$, $\Delta p\mathrm{K} = 8$. At the isoelectric point, the bulk and surface pH values are equal since there is no electric double-layer present. As we increase $p\mathrm{H}_b$ above the isoelectric point of the nanochannel up to neutral $p\mathrm{H}_b$, $p\mathrm{H}_s$ increases, but at a much slower rate than $p\mathrm{H}_b$. The value of $p\mathrm{H}_s$ saturates in the range of $p\mathrm{H}_b$ between 5 and 7. The saturation of $p\mathrm{H}_s$ occurs over a wider range of $p\mathrm{H}_b$ for smaller nanochannels since smaller nanochannels have a larger surface area to volume ratio. The resistance of the surface $p\mathrm{H}_s$ to change is due to the channel surface acquiring a negative charge, this negative charge in turn attracts of H_3O^+ ions towards the surface facilitating the reactions given in Eq. (1.8). As we continue to increase $p\mathrm{H}_b$ above neutral pH, there is an abrupt change in slope. This change in slope is due to a change in the pH controlling species from HCl to KOH.

In Fig 2.2(b) the charge regulating surface properties are, $p\mathrm{I} = 8$, and $\Delta p\mathrm{K} = 4$. Similar to Fig. 2.2(a) we observe strong buffering of the surface pH with respect to the bulk pH between neutral pH, and the isoelectric point of the channel surface. The buffering however extends over a larger range, from approximately bulk pH 6–9. The reason for the larger range is the relatively small $\Delta p\mathrm{K} = 4$. The apparent absence

of a slope change in 2.2(b) at neutral bulk pH is due to small electrostatic potentials at the interface resulting from the small difference in pI= 8 and 7, and hence small concentrations at the surface.

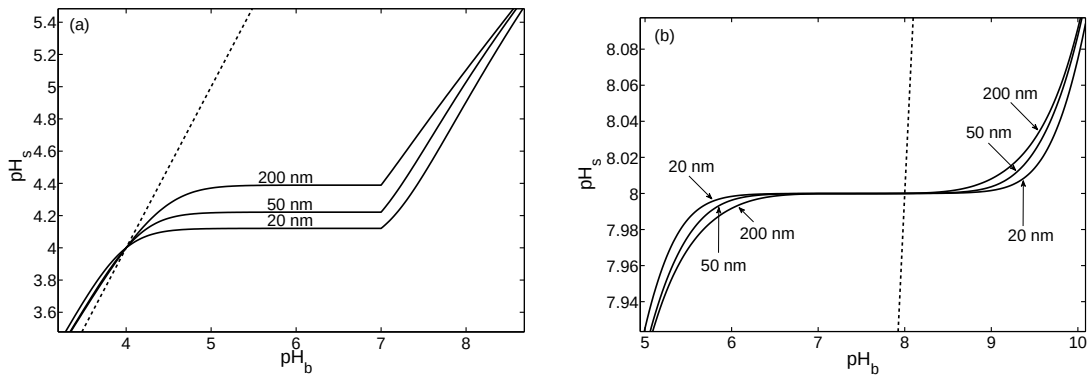

Fig. 2.2: Surface $p\mathrm{H}_s$ vs. bulk reservoir $p\mathrm{H}_b$ for various channel widths. (a) Corresponds to a surface with parameters, $p\mathrm{I} = 4$, and $\Delta p\mathrm{K} = 8$, and (b) corresponds to a surface with parameters $p\mathrm{I} = 8$, and $\Delta p\mathrm{K} = 4$. The dashed line in each figure corresponds to the bulk limit where no buffering is present, that is, $p\mathrm{H}_b = p\mathrm{H}_s$.

Fig. 2.3 shows a saturation in γ_c corresponding to two different sets of charge regulating parameters. In Fig. 2.3(a) the parameters correspond to $p\mathrm{I} = 4$ and $\Delta p\mathrm{K} = 8$. We observe a roughly constant conductivity for all channel sizes in the range, $5 < p\mathrm{H}_b < 7$. The region of constant conductivity is due to a buffering effect that takes place between the isoelectric point of the surface and neutral $p\mathrm{H}_b$. As the $p\mathrm{H}_b$ is increased from neutral, we see a small dip in conductivity. We discuss this dip in Section 2.3.3.

There are three major contributors to the $p\mathrm{H}_b$ range of the conductivity plateau. In general, the further the isoelectric point is from neutral $p\mathrm{H}_b$ the stronger the buffering effect is. At the isoelectric point, there will be no buffering, thus if a surface material has an isoelectric point at neutral $p\mathrm{H}_b$, we expect that it will not exhibit surface buffering effects. The size of the conductivity plateau is proportional to the difference of the materials isoelectric point and neutral $p\mathrm{H}_b$, i.e., $|p\mathrm{I} - 7|$.

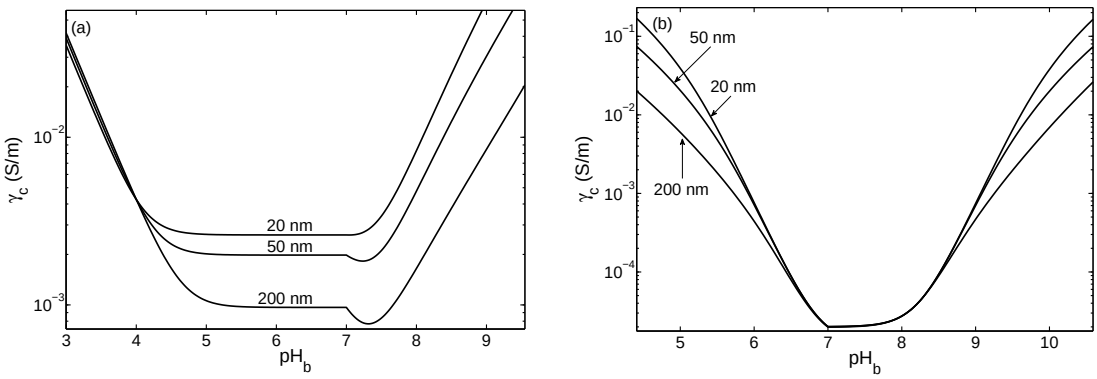

Fig. 2.3: Plots of channel conductivity vs. $p\mathrm{H}_b$ for various channel widths. These plots illustrate conductivity saturation for parameters, (a) $p\mathrm{I} = 4$, and $\Delta p\mathrm{K} = 8$, and (b) $p\mathrm{I} = 8$, and $\Delta p\mathrm{K} = 4$.

As the size of the nanochannel is increased, we see a general trend towards less buffering. Increasing channel size can be thought of as increasing the volume of the electrolyte to be buffered, while the buffering surface maintains a constant surface area. The remaining major contributor to surface buffering is the quantity $\Delta p\mathrm{K}$. As $\Delta p\mathrm{K}$ increases we see a general reduction in the buffer capacity of the surface.

In the range between the isoelectric point and neutral $p\mathrm{H}_b$, the absolute conductivity remains nearly constant because the surface acts as a buffer and keeps the concentration of counter ions (which dominate charge transport) nearly constant.

2.3.2 Effect of isoelectric point and $\Delta p\mathrm{K}$ on conductivity

The isoelectric point at the interface dictates the $p\mathrm{H}_b$ where the surface will have zero net charge and surface potential. Since there is no electric double layer when $p\mathrm{H}_b = p\mathrm{H}_s = p\mathrm{I}$ the model recovers bulk behavior. The difference between the bulk $p\mathrm{H}$ and the isoelectric point largely determines the surface potential. Larger differences in $p\mathrm{H}_b$ from $p\mathrm{I}$ result in larger surface potentials.

The channel surface is characterized by an intrinsic $\Delta p\mathrm{K}$ see Eq. (1.13). This

quantity controls the sensitivity of the surface potential Ψ_s to the double-layer overlap and roughly determines how many surface groups can bind or release H^+ at any given $p\mathrm{H}_b$ [99]. In Fig. 2.4 we consider the normalized conductivity $\gamma^* = \gamma_c/\gamma_b$, and how γ^* depends on $p\mathrm{H}_b$ and $\Delta p\mathrm{K}$. The quantity γ^* is the ratio of the conductivity from its bulk value due to the presence of the electric double layer in the nanochannel. Computations were performed for three different values of pI: 4, 7, and 10. Each curve is computed in the physically appropriate range where the concentration of the counter-ions at the surface is always < 0.1 M. Above the isoelectric point $\Delta p\mathrm{K}$ increases from top to bottom.

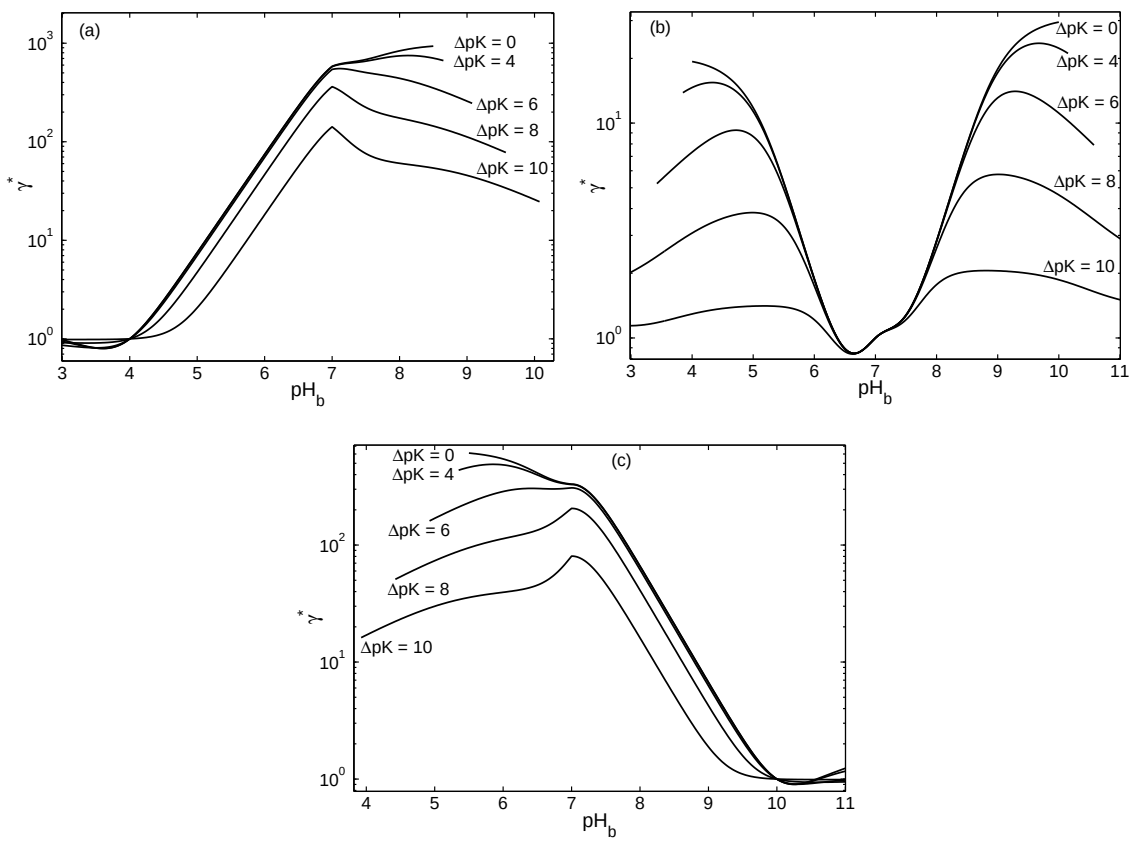

Fig. 2.4: Normalized channel conductivity in a 100 nm channel as a function of $p\mathrm{H}_b$ and $\Delta p\mathrm{K}$. (a) Corresponds to a surface isoelectric point, $p\mathrm{I} = 4$, (b) $p\mathrm{I} = 7$, and (c) $p\mathrm{I} = 10$.

Fig. 2.4(a) corresponds to $p\mathrm{I} = 4$. We see a roughly exponential decrease in normalized conductivity between $p\mathrm{H}_b = 4$ and $p\mathrm{H}_b = 7$. In this range, there is no electrostatic repulsion between the potential determining ion (in this region H^+) and the channel wall which leads to a buffering effect from the walls on the solution in the channel [96]. Indeed, the $p\mathrm{H}_s$ variations for the solution inside the channel are insignificant for variations of $p\mathrm{H}_b$ between the isoelectric point and 7. The buffering capacity increases with a reduction of $\Delta p\mathrm{K}$. For $p\mathrm{H}_b < 4$ we largely recover bulk behavior, but there are additional phenomena in this region discussed in Section 2.3.3. For $p\mathrm{H}_b > 7$ the surface has a strong negative charge, which results in K^+ being attracted into the channel and becoming the predominant charge carrier. The increase in K^+ ions is offset by a near complete elimination of H^+. As $p\mathrm{H}_b$ increases, the total number of OH^- ions increases, but they are largely expelled from the channel. The combination of all these effects leads to the observed drop in the conductivity when the $p\mathrm{H}_b$ is very slightly greater than 7, see Fig. 2.7.

Fig. 2.4(b) corresponds to $p\mathrm{I} = 7$. As the bulk $p\mathrm{H}_b$ is increased from neutral to approximately 9, we observe an increase in normalized conductivity. In this domain, the surface has a small negative charge partially expelling OH^- ions, and attracting K^+ ions.

The ionic concentration in a charged channel is always greater or equal than in the bulk reservoir. Higher ionic concentrations lead to higher conductivities. However, as the $p\mathrm{H}_b$ (and therefore total ionic concentration) is further increased this double layer effect is reduced due to charge screening, and the solution in the channel approaches the conductivity in the bulk reservoir.

Fig. 2.4(c) is qualitatively a mirror image of 2.4(a) with respect to $p\mathrm{H}_b = 7$. Again, in the region between $p\mathrm{H}_b = 7$, and the isoelectric point, the normalized conductivity has an exponential dependence with $p\mathrm{H}_b$. The quantitative differences between these figures are due to differences in diffusion constants for the various ions,

and will be discussed further in Section 2.3.3.

Surface effects are known to enhance conductivity in many cases due to a larger total number of ions being present in the double layer compared to the bulk [71]. The effects of surface conduction enhancement are illustrated in Fig. 2.5. For parameters $p\mathrm{I} = 4$, and $\Delta p\mathrm{K} = 8$, we observe increases in normalized conductivity near neutral $p\mathrm{H}_b$ as shown in Fig. 2.5(a). At a $p\mathrm{H}_b = p\mathrm{I} = 4$, γ^* is unity. The normalized conductivity greatly increases for $p\mathrm{H}_b$ values near neutral, and at neutral $p\mathrm{H}_b$ we observe a maximum. Additionally, we can see the effect of double layer overlap on conductivity since smaller channels have larger normalized conductivities. The cusp at $p\mathrm{H}_b = 7$ is due to a change in the $p\mathrm{H}$ determining electrolyte from HCl to KOH. For parameters $p\mathrm{I} = 8$ and $\Delta p\mathrm{K} = 4$, as shown in Fig. 2.5(b) we observe very different behavior. Since the isoelectric point of 8 is near neutral, the surface potentials are small near neutral $p\mathrm{H}_b$ resulting in only small increases in channel conductivity. As the $p\mathrm{H}_b$ is increased, or decreased from the isoelectric point, the surface potential increases, and in general the normalized conductivity also increases on the order of 10–100 at a $p\mathrm{H}_b$ of 5.

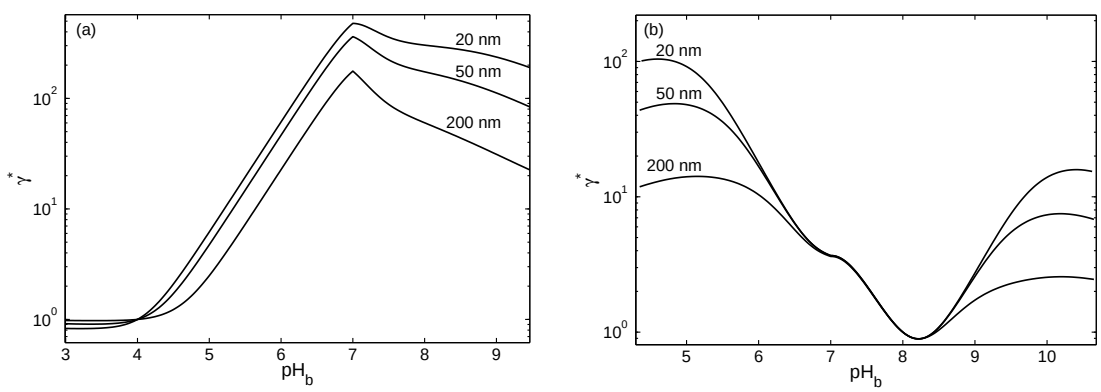

Fig. 2.5: Plots of normalized conductivity vs. $p\mathrm{H}_b$ for various channel widths, and charge regulating surface properties, (a) $p\mathrm{I} = 4$, and $\Delta p\mathrm{K} = 8$, and (b) $p\mathrm{I} = 8$, and $\Delta p\mathrm{K} = 4$.

2.3.3 Channel Conductivity Reduction

There are particular conditions that give rise to channel conductivities that are *lower* than their bulk values, and conditions that give rise to a *decrease* in conductivity when increasing ionic concentration. These results are counterintuitive because they involve a *decrease* in conductivity with an *increase* in total ion concentration inside the channel. In both cases, the reason for conductivity reduction is due to the difference in diffusion constants (i.e. mobilities) of the particular ionic species responsible for charge transport.

Conductivity reduction near isoelectric point

The first type of conductivity reduction occurs in the vicinity of the isoelectric point of the surface shown in Fig. 2.6. Fig. 2.6(a) corresponds to parameters, $p\mathrm{I} = 4$, and $\Delta p\mathrm{K} = 8$. In the region where the $p\mathrm{H}_b$ is near, but below the isoelectric point the surface becomes positively charged with a small surface potential and charge. This attracts negative counter-ions, which in our case are Cl^-, and repels H^+. This results in a slightly larger concentration of Cl^- ions than H^+ ions, the former having much smaller diffusion constants than the latter. Hence, even though the total concentration of ions is larger than that in the bulk, the conductivity goes down because we are exchanging faster H^+ ions with slower Cl^- ions.

Fig. 2.6(b) corresponds to parameters, $p\mathrm{I} = 8$, and $\Delta p\mathrm{K} = 4$. This case is very similar to what we observe in Fig. 2.6(a), however the isoelectric point is now in the alkaline region. As $p\mathrm{H}_b$ increases beyond 8, the surface becomes negatively charged, and attracts K^+ ions, while repelling OH^- ions. Since K^+ ions are slower than OH^- ions, the total conductivity of the channel drops below the bulk value.

For channel surfaces with large $\Delta p\mathrm{K}$ values, the effect of conductivity reduction is still present, but less pronounced. Small $\Delta p\mathrm{K}$ corresponds to an increase in buffer-

ing, which further decreases the concentration of H_3O^+ or OH^-, while large ΔpK effectively resembles large channel widths which results in approaching bulk behavior (see Section 2.3.2).

By rearranging Eq. (2.1) and Eq. (2.2) ignoring the electro-osmotic term, so that $\gamma_s < \gamma_b$ we can obtain the following criterion for the presence of conductivity reduction due to ionic mobility variations

$$\frac{D_+}{D_-} > \frac{1}{h}\int_{-h/2}^{h/2} \exp\left[\frac{e\Psi(x)}{k_B T}\right] dx. \tag{2.5}$$

Here D_+ is the diffusion constant of the positive ion, and D_- is the diffusion constant of the negative ion. In the case where $D_+ = D_-$ the channel conductivity will be greater than or equal to the bulk value for all non-zero channel potentials. Eq. (2.5) is valid for arbitrarily high potentials. It is worth noting that if the diffusion constants of the positive, and negative ions are very different, conductivity reduction may occur farther away from the isoelectric point where the surface potential is not necessarily small.

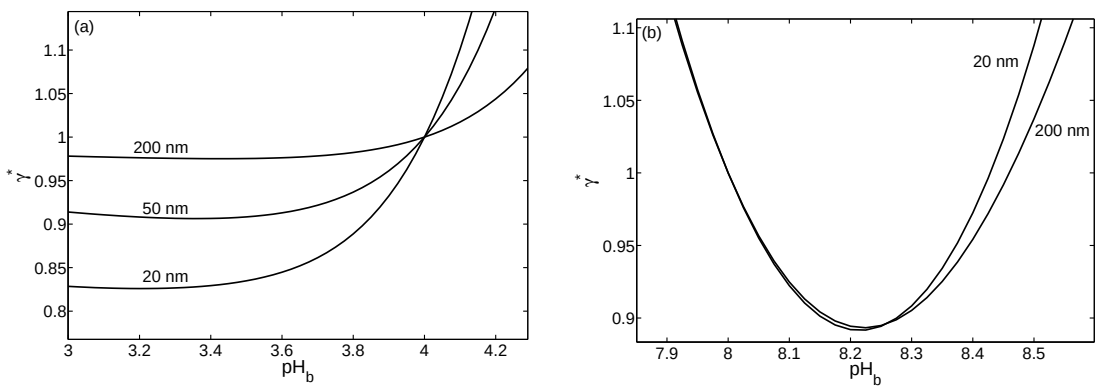

Fig. 2.6: Plots of normalized conductivities vs. $p\mathrm{H}_b$ for various channel widths, and that demonstrate conduction reduction for parameters (a) $p\mathrm{I} = 4$, and $\Delta p\mathrm{K} = 8$, and (b) $p\mathrm{I} = 8$, and $\Delta p\mathrm{K} = 4$.

Conductivity reduction near neutral $p\mathrm{H}_b$

The second type of conduction reduction occurs in the region near neutral $p\mathrm{H}_b$. Here it is instructive to look at the channel conductivity rather than the normalized conductivity, see Fig. 2.7.

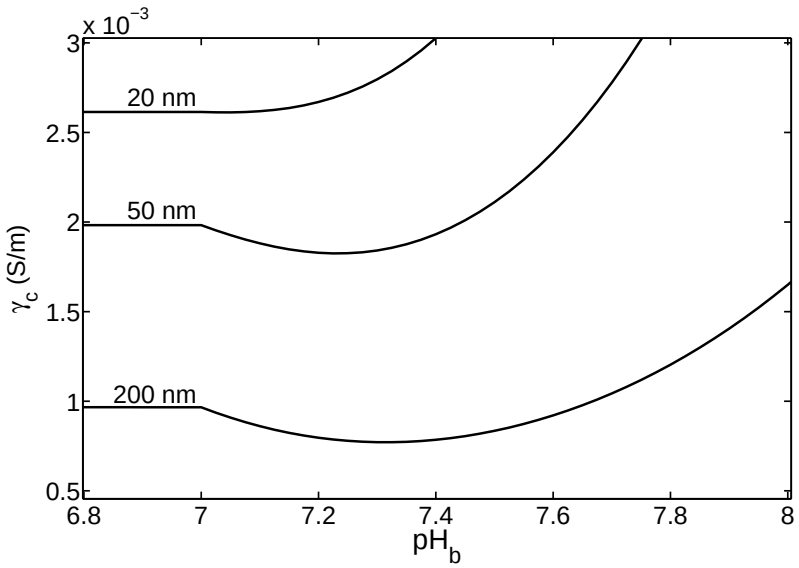

Fig. 2.7: Plots of channel conductivities vs. $p\mathrm{H}_b$ for channels of various widths with parameters $p\mathrm{I} = 4$, and $\Delta p\mathrm{K} = 8$.

Consider the case where $p\mathrm{I} < 7$. As shown in Section 2.3.2 the range of $p\mathrm{H}_b$ between the isoelectric point and $p\mathrm{H} = 7$ is characterized by fairly constant conductivity due to surface buffering effects. However, as the $p\mathrm{H}_b$ value increases above 7 through addition of KOH, we observe an abrupt decrease in the channel conductivity despite the fact that we are increasing the ionic strength of the solution, see Fig. 2.7. This decrease typically happens over a short range (less than one $p\mathrm{H}$ unit) after which the conductivity increases above the conductivity of pure water.

At $p\mathrm{H}_b = 7$ for a surface with $p\mathrm{I} = 4$, there is a very strong double layer overlap due to very small ionic concentrations 10^{-7} M. At a $p\mathrm{H}_b = 7$, there is a large difference between $p\mathrm{H}$ and the isoelectric point which results in a large negative potential. This

large potential expels nearly all the OH^- ions from the channel.

As small amounts of KOH are added to the bulk solution to increase the $p\mathrm{H}_b$ from 7 to approximately 7.35, nearly all the OH^- ions are expelled from the channel, but the K^+ ions remain inside the channel. The change in $p\mathrm{H}_b$ is not enough to significantly alter the surface potential (or surface charge), which results in K^+ ions displacing H_3O^+ ions. Since K^+ ions have smaller diffusion constants than H_3O^+ ions, the conductivity goes down.

This is a different from the conduction reduction described in the previous section where the normalized conductivity goes down due to the ratio of D_+/D_-. The current phenomenon is due to a ratio of similarly charged ions e.g. $D_{\mathrm{K}^+}/D_{\mathrm{H_3O}^+}$ and their relative concentrations. This effect exhibits a maximum with respect to channel dimension and $\Delta p\mathrm{K}$, see Fig. 2.8.

Fig. 2.8 illustrates the minimum normalized conductivity and optimal $p\mathrm{H}_b$ vs. channel width. In this case the minimum normalized conductivity is the smallest conductivity divided by the conductivity of the same channel with neutral $p\mathrm{H}_b$. we can achieve by varying the $p\mathrm{H}_b$ above 7 for a particular channel width. The optimal $p\mathrm{H}_b$ is where we see the largest drop in conductivity. In the limit of large channels we expect to see the normalized conductivity approach 1, and optimal $p\mathrm{H}_b = 7$. We observe a global minimum in the conductivity normalized with respect to the channel conductivity at neutral $p\mathrm{H}$, $\gamma_c^N \approx 0.75$ for a channel width of 1.2 μm and $p\mathrm{H}_b$ of 7.35.

2.4 Conclusion

The surface chemistry at the walls of fluidic nanochannels is extremely important for the transport of ionic species under the action of externally applied electric field. The system, analyzed in this chapter consists of a fluidic nanochannel that is connected to

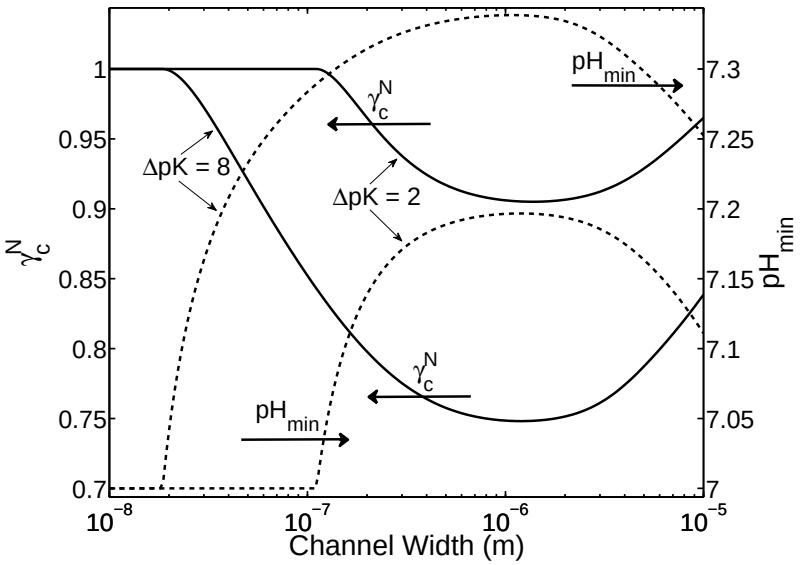

Fig. 2.8: Plot of conductivity normalized with respect to the channel conductivity at neutral pH, $\gamma_c^N = \gamma_c/\gamma_N$, where γ_N is the conductivity inside the channel at neutral pH, i.e., $\gamma_N \equiv \gamma_c(p\mathrm{H} = 7)$. Two systems are represented one with charge regulation parameters, $p\mathrm{I} = 4$, and $\Delta p\mathrm{K} = 8$, and the second with parameters, $p\mathrm{I} = 4$, and $\Delta p\mathrm{K} = 2$. Solid lines represent γ_c^N with the axis on the left side, while dashed lines represent $p\mathrm{H}_{\mathrm{min}}$ (the pH of the bulk reservoir where conductivity is minimized) with the axis on the right side.

infinitely large external reservoirs with controlled $p\mathrm{H}_b$. The large surface area volume ratio of the channel leads to a significant buffering effect that is due to charge regulation (e.g., binding or releasing of H_3O^+ ions) that occurs at the solid-liquid interface. The buffering is most noticeable in the range between the surface isoelectric point and $p\mathrm{H}_b = 7$. In this range the system exhibits a constant surface charge, but that condition is not uniformly applicable. The buffering also depends on the difference between the pK values for the two principal surface chemical reactions ($A^- + H_3O^+ \rightleftharpoons AH$ and $AH + H_3O^+ \rightleftharpoons AH_2^+$). An interesting result is that the quantity $\Delta p\mathrm{K}$ behaves similarly, though not identically to that of the channel width. The complex combination of surface chemistry and ionic mobilities sometimes leads to counterintuitive drops in the local conductivity even if the overall electrolyte concentration is going up. These drops take place near the isoelectric point of the surface or around

$p\mathrm{H}_b = 7$. In the first case this is attributed to the different mobilities of the present positive and negative ions, while the latter is due to the mobility differences between the potential determining and indifferent counterions. The analysis presented in this chapter clearly demonstrates the important role that the surface chemistry and charge regulation plays on the ionic transport in very narrow channels. While the focus is on current transport other electrokinetic phenomena like electroosmosis will be affected in a similar way.

Chapter 3

Charge Regulation at Semiconductor-Electrolyte Interfaces

Semiconductor colloids are of significant fundamental interest and present opportunities for new and exciting applications [86, 88]. A basic property pertinent to any colloidal system is its stability. Semiconductor colloids are no different. Strategies to stabilize such systems employ electrostatic and/or steric [87, 100] repulsion against van der Waals attraction to prevent the particles from coagulation. The balance between electrostatic repulsion and van der Waals attraction is the foundation of the celebrated Derjaguin-Landau-Verwey-Overbeek (DLVO) theory of colloid stability [3, 101]. We find that the charge density in the doped semiconductor particle interior plays an essential role and can significantly alter the overall interaction. It has been experimentally established that the charge density inside a doped semiconductor in the vicinity of semiconductor-electrolyte interface will shift in response to changes in the electrostatic potential in the electrolyte phase. This effect has been exploited to perform force measurements [76, 77] and is utilized in a significant

number of sensing applications that use nanoscale semiconductors [79, 80, 102–106].

We hypothesize that the internal charge redistribution due to external field perturbation should in turn affect the force between two approaching semiconductor colloidal particles. Hence, the DLVO theory has to be revisited when applied to doped semiconductor colloids. In this chapter we provide such a revision based on a general electrostatic analysis. We show that the internal response of the doped semiconductor particles to changes of the potential in the electrolyte may have a dramatic effect on their kinetic stability. In addition, it opens up possibilities to new methods for control and manipulation.

We begin by considering a semiconducting colloidal particle suspended in electrolyte solution. In order to be specific let the particle have a Si core (other semiconductors will perform similarly) and the terminal ligands at the surface are $-\,\mathrm{SiO^-}$ groups [87]. Such oxide layer may naturally form when Si is exposed to air or water that has dissolved oxygen. The $-\mathrm{SiO^-}$ groups are subject to surface charge regulation [20,107,108] through chemical equilibria with constants K_- and K_+. We modify the chemical equilibria given in Eq. (1.8) to replace the amphoteric $\mathrm{A^-}$ groups with $-\mathrm{SiO^-}$ groups so that

$$\begin{aligned} \mathrm{SiOH_2^+ + H_2O} &\rightleftharpoons \mathrm{SiOH + H_3O^+}, \quad p\mathrm{K_+} = -\log_{10}\mathrm{K_+} \\ \mathrm{SiOH + H_2O} &\rightleftharpoons \mathrm{SiO^- + H_3O^+}, \quad p\mathrm{K_-} = -\log_{10}\mathrm{K_-}. \end{aligned} \tag{3.1}$$

We will assume (without loss of generality) that the core is n-doped. The potential Ψ in the two domains is described by the Poisson equation Eq. (1.1) [109]

$$\nabla^2\Psi = -\frac{\rho}{\varepsilon_r\varepsilon_0}. \tag{3.2}$$

In contrast, the charge distribution density in the doped semiconductor particle core is subject to quantum exclusion limitations and may have to be described by a temperature dependent Fermi-Dirac distribution [110, 111]. The charge densities are

similar to that given by Eq. (1.2) but are now dependent on the phase of the material. The necessary modifications for the charge densities are given as

$$\rho = \begin{cases} \sum_i e n_i^0 z_i \exp\left(\frac{-z_i e\Psi}{k_B T}\right) & \text{electrolyte} \\ eN_d\left[1 - \chi F_{1/2}\left(\frac{\mu - e\Psi}{k_B T}\right)\right] & \text{semiconductor} \\ 0 & \text{oxide,} \end{cases} \tag{3.3}$$

where N_d is the number density of donors in the semiconductor, and $\hbar$ is the reduced Planck constant. $F_{1/2}$ is the Fermi integral and is defined as

$$F_{1/2}(x) = \frac{2}{\sqrt{\pi}} \int_0^\infty dt \frac{t^{1/2}}{1 + \exp(t - x)}, \tag{3.4}$$

where μ is the Fermi level [111], and the parameter χ is given by

$$\chi = \frac{1}{4N_d}\left(\frac{2m^* k_B T}{\pi\hbar^2}\right)^{3/2}, \tag{3.5}$$

where m^* is the effective mass of the electron. The charge density inside the oxide layer is zero. Since we are considering a system at room temperature, it is appropriate to use the limiting case of the Fermi function where

$$\chi F_{1/2}\left(\frac{\mu - e\Psi}{k_B T}\right) \to \exp\left(-\frac{e\Psi}{k_B T}\right). \tag{3.6}$$

The boundary conditions required to solve Eq. (3.2), are to match potentials at the interfaces of the semiconductor (subscript "sc"), oxide (subscript "ox") and electrolyte (subscript "el") such that the charge regulating boundary condition is enforced at the oxide-electrolyte interface through

$$\Psi_{ox} = \Psi_{el} = \Psi_s; \sigma_s = \mathbf{n} \cdot \left[\varepsilon_{\text{ox}} \left(\nabla\Psi\right)_{\text{ox}} - \varepsilon_{\text{el}} \left(\nabla\Psi\right)_{\text{el}}\right], \tag{3.7}$$

while the boundary conditions applied at the semiconductor-oxide interface are

$$\Psi_{sc} = \Psi_{ox}; 0 = \mathbf{n} \cdot \left[\varepsilon_{\text{sc}} \left(\nabla\Psi\right)_{\text{sc}} - \varepsilon_{\text{ox}} \left(\nabla\Psi\right)_{\text{ox}}\right], \tag{3.8}$$

where σ_s and Ψ_s are the surface charge and potential governed by the chemical equilibria given in Eq. (3.1), $\mathbf{n}$ is the vector normal to the surface, and ε_{sc}, ε_{ox}, ε_{el} are the dielectric constants of the semiconductor, oxide and electrolyte respectively.

In this model we use a site dissociation model such that the charge density is given by [20, 21],

$$\sigma_s(\Psi_s) = \frac{e\Gamma\delta \sinh[e(\Psi_N - \Psi_s)/k_BT]}{1 + \delta \cosh[e(\Psi_N - \Psi_s)/k_BT]}. \tag{3.9}$$

The spatial dependence of the electrostatic potential Ψ and charge density ρ on the distance between two particles with a separation of 10 nm and a particle in isolation is shown in Fig. 3.1. The results presented in the figure were obtained by numerically solving Eqs. (3.2) and (3.3). Alternatively the exact analytical solution of Behrens and Borkovec [22] for interacting surfaces with charge regulation can be adapted to obtain the same results. As the distance between the charged particles varies, the potential distribution changes in the electrolyte filled gap between the surfaces as well as in the particle interior. This is due to the fact that the potentials inside and outside of particles are connected through Eqs. (3.7) and (3.8). The coupling goes both ways, hence the potential and charge distributions in the electrolyte will be affected by the fact that inner charges respond by internal redistribution to the particle approach.

3.1 Charge regulation at an isolated semiconductor electrolyte interface

The electrostatic potential distribution for a doped semiconductor-oxide-electrolyte system is shown in Fig. 3.2. It illustrates the effect of the doping level on the potential distribution in all phases. The oxide layer is charge-free and acts as a capacitor.

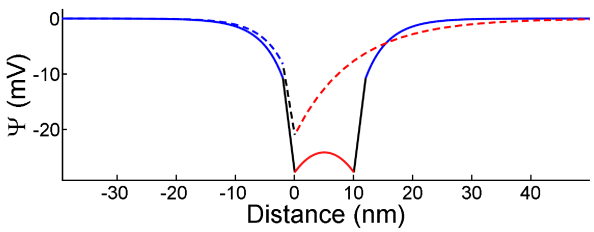

Fig. 3.1: One dimensional potential distributions in the electrolyte solution (red), oxide layer (black), and the semiconductor (blue) approximated as infinite flat plates. The solid line corresponds to two particles separated by 10 nm, while the dashed line corresponds to the potential distribution of a single particle in isolation. These curves illustrate how the potential distribution inside the semiconductor responds to the presence of an approaching colloid. The particles are covered with $-\mathrm{SiO}^-$ groups with surface density $\Gamma = 8\times10^{18}$ m^{-2}. These groups may release or attach a proton according to Eq. (3.1). The parameters for this calculation are: $p\mathrm{H} = 3.5$, the overall electrolyte concentration is 0.925 mM (adjusted by adding symmetric monovalent electrolyte), $p\mathrm{K}_+ = -2$, $p\mathrm{K}_- = 6$, and the particle doping is 10^{24} m^{-3}. The dielectric permitivities were $\varepsilon_{\mathrm{el}} = 78.5$ for the electrolyte, $\varepsilon_{\mathrm{sc}} = 11.7$ for Si, and $\varepsilon_{\mathrm{ox}} = 3.9$ for the 2 nm thick layer of SiO_2 [1, 2].

The figure also demonstrates that the surface potential at the oxide-electrolyte interface varies moderately with doping. The effect of doping has a dramatic effect on the potential distribution inside the semiconductor because of screening, but a relatively small effect on the potential distribution in the electrolyte. It is interesting to note however, that while doping seems to have only minor effect on the potential distribution in the electrolyte for a single interface, it plays a significant role if a second charged interface is present. As a second charged object approaches, the doping in the semiconductor enhances the lowering of the surface potential at the interface, thus reducing the overall repulsion (see Section 3.2 below).

In contrast to the doping effect, varying the electrolyte concentration significantly changes the electrostatic potential everywhere (see Fig. 3.3). The drop of the potential with the electrolyte concentration is very pronounced. The reason for this strong effect is due to the fact that the charge regulating surface groups are exposed to the electrolyte solution and chemically interact with the potential determining

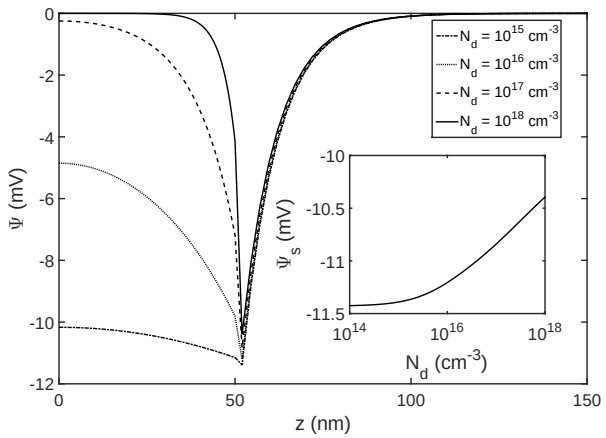

Fig. 3.2: Potential distributions plotted as a function of distance z. The semiconductor/oxide interface is at $z = 50$ nm while the oxide/electrolyte interface is at $z = 52$ nm. The various lines depict varying doping concentrations. The inset is a plot of surface potential Ψ_s versus doping N_d.

ions there [see Eq. (3.1)]. The surface charge σ_s is strongly affected by changes in the electrolyte such as potential screening due to the variation of the salt concentration, which leads to a change in the potential distribution also in the semiconductor phase (across the capacitive oxide layer). Details on calculating the surface charge density when using Fermi-Dirac statistics are given in Appendix C.

Fig. 3.4 illustrates the effect of the surface chemistry on the electrostatic potential distributions. The surface chemistry effect is complex and depends on the chemical structure of the interface as well as on the composition of the solution. The surface groups have an affinity to particular ionic species (the potential determining ions, in this case H_3O^+) and the main characteristic of this interaction is quantified by the equilibrium constants or the ΔpK values [see Eq. (3.1)]. The difference between ΔpK in conjunction with the pH determines how charged the surface would be as a result of the chemical reactions in Eq. (3.1). That is why the electrostatic potential distributions in both the semiconductor and electrolyte phases are strong functions

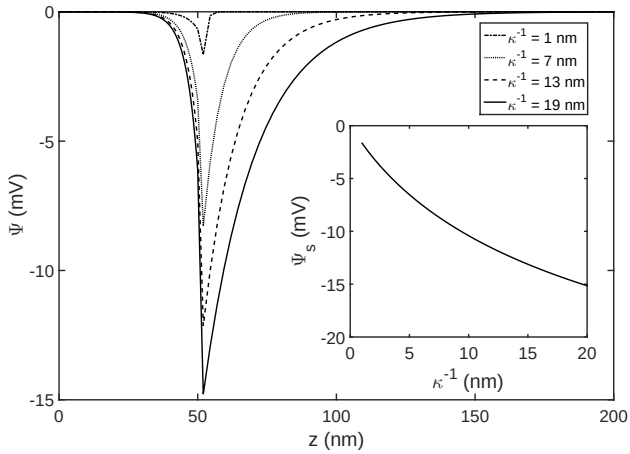

Fig. 3.3: Potential distributions plotted as a function of distance z. The parameters are the same as those given in Fig. 3.2 but at constant doping of $N_d = 10^{18} cm^{-3}$. The inset is a plot of the surface potential Ψ_s versus Debye length κ^{-1}.

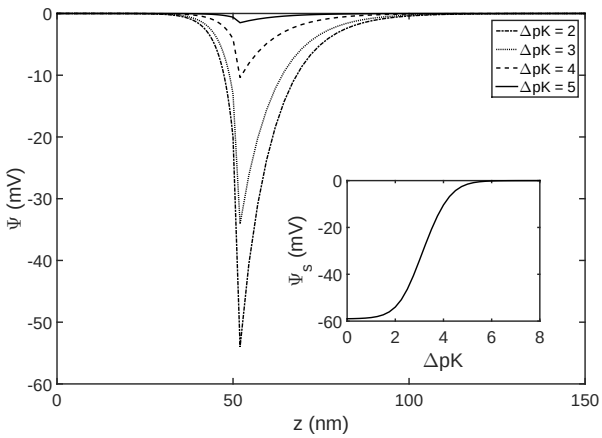

Fig. 3.4: Potential distributions plotted as a function of distance z for different values of ΔpK. The parameters are the same as those given in Fig. 3.2 but at constant doping of $N_d = 10^{18}\ cm^{-3}$. The inset shows surface potential versus ΔpK.

of ΔpK. Varying the surface chemistry and hence, the value of ΔpK is possible only by deliberate surface modification, and might be an experimentally non-trivial task

for certain materials. Still, it is interesting to know how the global electrostatics are impacted by the specific chemical groups exposed at the interface with the electrolyte solution. The results shown in Fig. 3.4 suggest that as $\Delta p\mathrm{K}$ decreases, the magnitude of electrostatic potential in all phases increases. It is important to note that the $p\mathrm{H}$ of the solution is one unit higher than the isoelectric point, which is the same for all cases, i.e., $p\mathrm{I} = 2$. Note that for $\Delta p\mathrm{K} = 2$, $p\mathrm{H} = p\mathrm{K}_-$. For $\Delta p\mathrm{K} = 0$ the surface potential becomes $\Psi_N = \Psi_s \approx 60$ mV. In the other extreme when $\Delta p\mathrm{K}$ is large, the magnitude of the surface charge tends to zero. The reason is that for large $\Delta p\mathrm{K}$, the values of $p\mathrm{K}_-$ and $p\mathrm{K}_+$ are so far away from the solution $p\mathrm{H} = 3$ that any of the reactions in Eq. (3.1) tend towards the neutral species.

3.2 Interaction between Semiconductor Colloidal Particles in Electrolyte Solution

Knowing the electrostatic potential distribution we can obtain the interaction energy between two semiconductor particles as described above in Section 3.1 (See Figs 3.5 and 3.6). We have obtained an energy plot in our previous work [93] using the so-called Derjaguin approximation [1, 101, 112], which is valid for particles with radius greater than the separation distance between them. Here we relax this limitation, by numerically integrating the disjoining pressure over the midplane separating the particles at different interparticle separations [see Eq. (A.1) and Fig. 3.5] to obtain the force vs distance relationship. Next we integrate the force over the distance to obtain the electrostatic energy of interaction. The van der Waals contribution given by Eq. (3.13) is added to it to obtain the total energy of interaction. The parameters for the computation are Hamaker constant $A_H = 5.4 \times 10^{-20}$ J, particle radius $a = 100$ nm, density of the surface charged groups $\Gamma = 8 \times 10^{18}$ m^{-2}, electrolyte concentration 0.925 mM, $p\mathrm{K}_+ = -2$, $p\mathrm{K}_- = 6$, particle doping 10^{18} cm^{-3} and dielectric

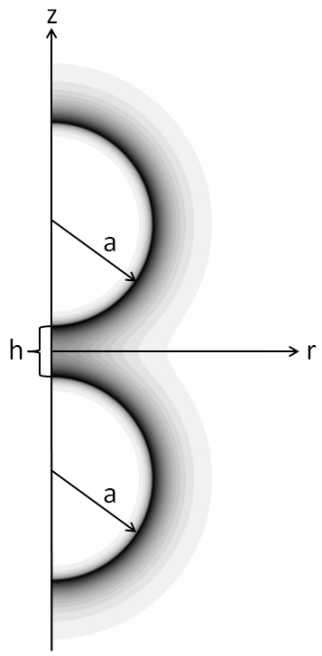

Fig. 3.5: Visualization of system consisting of two particles. Axis symmetry along z with the other spatial coordinate r results in the two particles being spherical in geometry. The separation of the particles is given as h, and the radius of the particles is a. The shaded portions represent the magnitude of the potential Ψ for a particular set of values, darker shades indicate larger values. It can be seen that the smallest values of Ψ are far from the particle surface in the electrolyte, as well as deep in the interior of the semiconductor particles. At this scale the oxide layer is too thin to be easily seen.

permittivities $\varepsilon_{\text{ox}} = 3.9$, $\varepsilon_{\text{el}} = 78.5$, and $\varepsilon_{\text{sc}} = 11.7$. The thickness of the oxide layer is 2 nm. The numerically obtained energy curve is very similar to the one derived using Derjaguin approximation [93]. However, there are some important differences. The Derjaguin approximation tends to overestimate the difference between the doped and undoped cases, as well as the magnitude of the secondary minimum at larger separations. Despite the reduction, there is still a significant difference between the energy barriers for the doped and undoped cases, which will have a significant effect on the stability [93]. The inset shows the difference between interaction energies for two n-doped, two p-doped and one n-doped particle interacting with a p-doped

one. The differences are due to the fact that the different mobile charges in the semiconductors will interact slightly differently with the always negatively charged interface. However, the main effects on the total interaction energy is primarily due to the charge mobility and much less to its polarity.

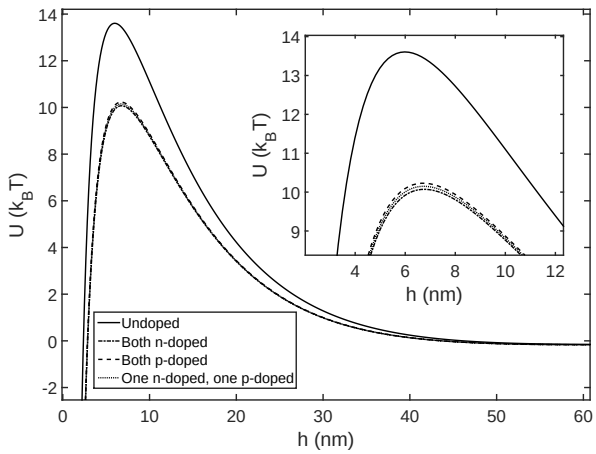

Fig. 3.6: Interaction energy versus separation h. The solid line is for two undoped particles, a noticeable reduction in free energy can be seen for the various combinations of doped particle interactions. The inset provides a closer look at the peak of the doped particle interaction energies.

Fig. 3.7 demonstrates the effect of the surface chemistry by plotting the energy-distance curves at different values for the parameter $\Delta p\mathrm{K}$. Larger values of $\Delta p\mathrm{K}$ reduce the energy of interaction and vice versa. These results are in agreement with those shown in Fig. 3.4. The isoelectric point of the surface is again $p\mathrm{I} = 2$ and the $p\mathrm{H} = 3$. As $\Delta p\mathrm{K}$ is increased the surface charge on both particles goes down, thus reducing the repulsion. Hence, the surface chemistry has a strong effect in the interaction energy between semiconductor colloids, very much like it has on interaction energy between dielectric particles in suspension. Still, there is a difference between doped and undoped particles. A greater $\Delta p\mathrm{K}$ value will generally destabilize doped particles more than undoped.

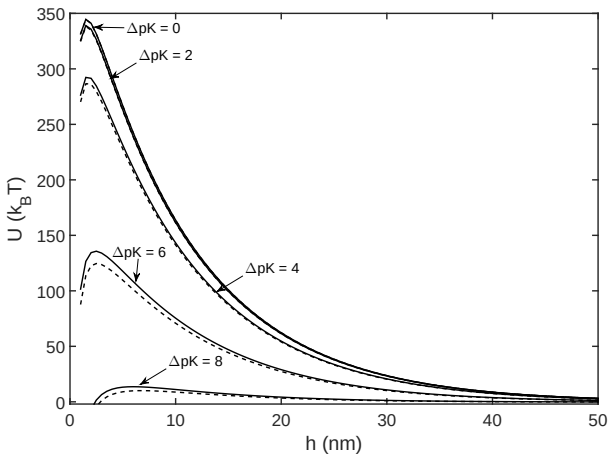

Fig. 3.7: Interaction energy versus separation h. The solid lines are for undoped spherical particles and the dashed lines are for their doped counterparts where $N_d = 10^{18}/cm^3$.

For highly doped systems where $T_F > T$ the approximation to Fermi statistics using an exponential as described in Eq. (3.6) breaks down. Fig. 3.8 illustrates how the potential distribution inside the semiconducting region is affected by the exponential approximation versus using the Fermi integral expression for the charge density distribution [see the second line in Eq. (3.3)]. Details explaining the solution procedure are given in Appendix D. At moderate doping concentrations of $N_d = 10^{18}/\text{cm}^3$ the potential distributions are very close, and as doping is decreased the exponential approximation is a very good one. However, at larger doping concentrations it can be seen that it is necessary to use the Fermi integral in the evaluation of the potential distribution. It interesting to point that the exponential (Boltzmann) approximation for doping level equal to $N_d = 10^{19}/\text{cm}^3$ is almost identical to the more accurate result based on the Fermi model for $N_d = 10^{20}/\text{cm}^3$. Hence, the approximate Boltzmann expression is completely inadequate at high levels of doping. The use of the Fermi integral at high doping also reveals that the reduction in the magnitude of the surface potential Ψ_s is less than predicted by the exponential approximation.

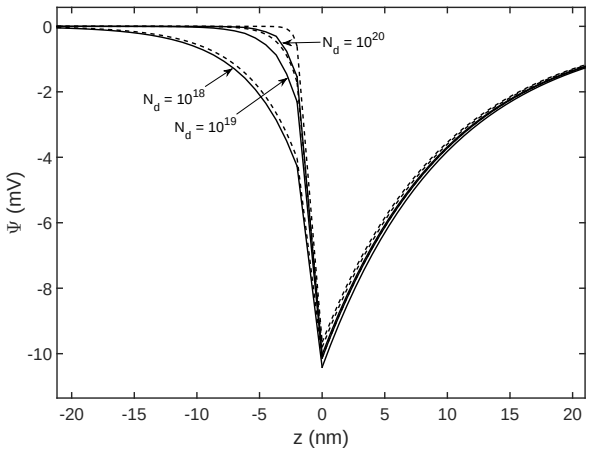

Fig. 3.8: Potential distributions of a one dimensional semiconductor-oxide-electrolyte system demonstrating the difference between the approximation described in Eq. (3.6). The dashed lines were calculated using Boltzmann statistics while the full lines were calculated by numerically evaluating the Fermi integral in Eq. (3.3).

Knowing the effect of separation on the potential and charge density distributions, in both particle interior and exterior, allows us to derive the pair electrostatic energy of interaction between the two spherical colloidal particles of radius a separated by distance h using the Derjaguin method [3, 101]

$$U_e(h) = \pi a \int_h^\infty dy \int_\infty^y dz \Pi_e(z), \tag{3.10}$$

where y and z are distance variables. A detailed description of the solution and the assumptions made are given in Appendix A, but we should emphasize here that the pressure Π_e depends on the electrostatic potentials, and hence on the separation distance. The total energy of interaction consists of [3, 101]

$$U(h) = U_e(h) + U_{\rm vdw}(h), \tag{3.11}$$

with $U_{\rm vdw}$ being the van der Waals attractive energy which for small separations between two parallel infinite flat plates is

$$U_{\rm vdw}(h) = -\frac{A_H a}{12h}, \tag{3.12}$$

and for between two spheres is

$$U_{\rm vdw}(h) = -\frac{A_H}{6}\left\{\frac{2a^2}{(h+2a)^2} + \frac{2a^2}{h^2+4ah} + \ln\left[\frac{h(h+4a)}{(h+2a)^2}\right]\right\}, \tag{3.13}$$

where A_H is the Hamaker constant [3, 19, 101].

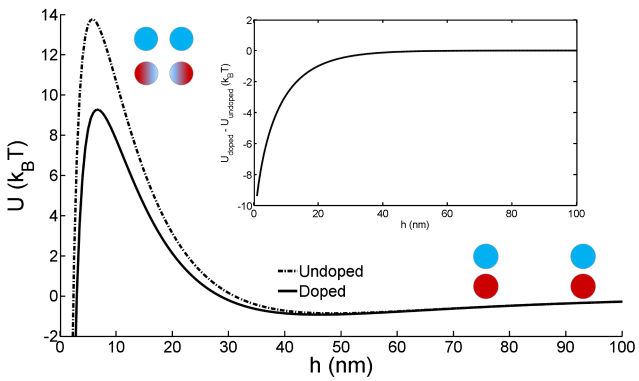

Fig. 3.9: Interaction between colloids. Interaction energy between undoped (blue particles, full line) and doped (red particles, dashed line) semiconductor colloids. As the particles approach the charge density in the doped particles redistribute which is illustrated by the gradual color change. The Hamaker constant used to generate this plots is $A_H = 5.4 \times 10^{-20}$ J, and the particle radius is a = 100 nm. The rest of the parameters are the same as in Figure 3.1. The inset shows the difference between the two energy curves.

The total interaction energy given by Eq. (3.11) is shown in Fig. 3.9. The height of the maximum determines the stability against coagulation. Overcoming the barrier brings the two particles into the region of very close separations where the van der Waals attraction completely overpowers the electrostatic repulsion and leads to irreversible coagulation. The difference between the energy maxima for doped and undoped semiconductor colloids, and the parameters listed in Figs. 3.1 and 3.9 is slightly more than 4 k_BT. It is due to fact that internal charge density redistribution in the doped semiconductor reduces the potential in the electrolyte gap between the particle surfaces. Hence, the electrostatic repulsion for doped particles is less than that for undoped, which leads to a different energy curve (see Fig. 3.9). The inset shows the energy change that is due to the doping. This is a new type of colloidal

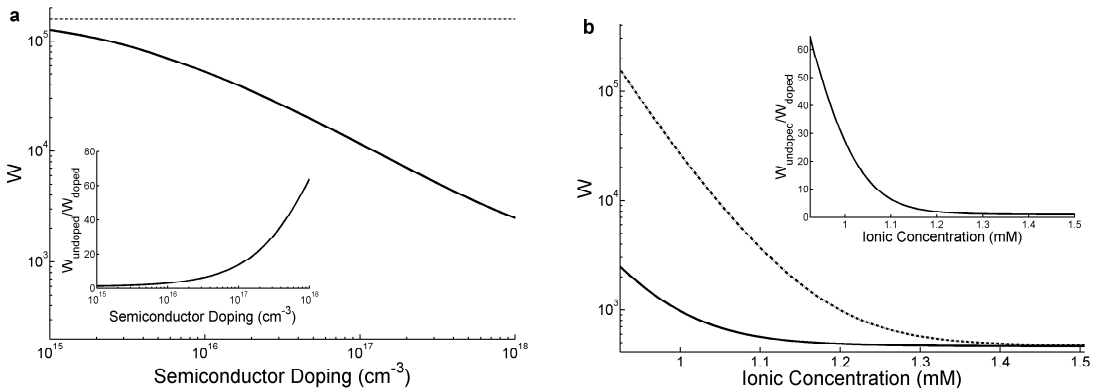

Fig. 3.10: Differences in stability due to doping. (a) Stability of undoped (dashed) and doped colloids (solid) vs. semiconductor doping concentration. The stabilities are useful for calculating time to coagulation. The inset shows relative stability $W_{\text{undoped}}/W_{\text{doped}}$ vs. doping. The relative stability is useful for calculating relative times to coagulation for undoped vs. doped particles. (b) Stability of undoped (dashed) and doped colloids (solid) vs. ionic concentration of the electrolyte. The relative stability $W_{\text{undoped}}/W_{\text{doped}}$ vs ionic concentration of the electrolyte is given in the inset. The rest of the parameters are the same as in Figs. 3.1 and 3.9

.

interaction that is uniquely characteristic to semiconductor colloids in aqueous suspension and is very significant in both magnitude and range. This effect depends on the doping concentration and decreases as the latter goes down and vice versa.

Suspensions characterized by a combination of van der Waals and electrostatic interactions are thermodynamically unstable and, given enough time, will ultimately coagulate. The energy barrier however provides kinetic stability that may allow for sufficient time for different applications and processing. The rate equation describing the coagulation of two colloidal particles (formation of doublets) is [112–114]

$$\frac{dn_2}{dt} = k_c n_1^2, \tag{3.14}$$

where n_2 is the concentration of coagulated pairs (doublets), n_1 is the concentration of single particles, t denotes time, and $k_c = k_0/W$ is the rate constant.

With k_0 we denote the rate constant in absence of any long range interactions and energy barriers (the rate is purely diffusion-limited). The effect of slowing down

due to the presence of an energy barrier is taken into account by the stability factor [112, 115, 116],

$$W = 4a \int_0^\infty \frac{H(h) \exp\left[U(h)/k_B T\right]}{h - 2a} dh, \tag{3.15}$$

where $H(h) = (4h + a)/4h$ embodies the hydrodynamic effects [117] (also see Appendix A)

$$\Psi_s = \frac{\Gamma \delta e \sinh(e\Psi_N/k_B T)}{[\delta \cosh(e\Psi_N/k_B T)+1]\left[\varepsilon_0 \varepsilon_{\rm el} \kappa_{\rm el} \tanh\left(\frac{\kappa_{\rm el} h}{2}\right) + \frac{\varepsilon_0 \varepsilon_{\rm ox} \epsilon_{\rm sc} \kappa_{\rm sc}}{\varepsilon_0 + L_{\rm ox} \varepsilon_{\rm sc} \kappa_{\rm sc}} + \frac{\Gamma \delta e^2 (\cosh(e\Psi_N/k_B T)+\delta)}{k_B T (\delta \cosh(e\Psi_N/k_B T)+1)^2}\right]}. \tag{3.16}$$

For the parameters in Figs. 3.1 and 3.9, the coagulation rate in an undoped sample will be more than 60 times slower than the doped sample (see Fig. 3.10). This is a significant difference that cannot be ascertained using the conventional DLVO theory. This new effect is entirely due internal mobility and reconfiguration of charges in the doped semiconductor. Fig. 3.10(a) illustrates how the stability factor W of the colloidal system depends on doping [see Eq. (3.15)]. The relative coagulation rate is shown in the inset. As the doping level increases, the doped system becomes more unstable and prone to coagulation and precipitation. Fig. 3.10(b) illustrates how a change in ionic concentration affects the stability of the colloids.

In the limit where the surface potential is small, $|\Psi_s| < 26$ mV we have derived Eq. (3.16) for the surface potential (see also Appendix B). The inverse Debye lengths are given as, $\kappa_{\rm sc} = \sqrt{n_{\rm sc} e^2/\varepsilon_{\rm sc} \varepsilon_0 k_B T}$ and $\kappa_{\rm el} = \sqrt{n_{\rm el} e^2/\varepsilon_{\rm el} \varepsilon_0 k_B T}$ for the semiconductor and electrolyte phases respectively where $n_{\rm sc}$ and $n_{\rm el}$ are the number densities of ions, also for the semiconductor and electrolyte phases respectively. Eq. (3.16) allows for the derivation of analytical expressions for the potential distributions in all phases. Further analysis provides insight into the functional form of the surface potential in various limits. In the low doping limit $\kappa_{\rm sc} \to 0$ we recover the equivalent expression for charge regulation at a dielectric-electrolyte interface. Similarly, when

the thickness of the oxide L_{ox} is large such that $L_{\text{ox}} \to \infty$ we again recover the expression for charge regulation at a dielectric-electrolyte interface. In the high doping, or metal-like limit where $\kappa_{\text{sc}} \to \infty$ and $L_{\text{ox}} \to 0$ the effect from the redistribution of charges in the semiconductor region is even stronger, as long as there is an oxide barrier to prevent the release of ions into solution. In the case of a metal-like particle without an oxide, the charge regulation formulas would have to be revisited.

The internal mobility of charges (electrons and/or holes) in semiconductor materials has been experimentally demonstrated and utilized in different sensing applications [76,77,79,84,86,88,102,104,105,118,119]. We used first principle continuum electrostatics [109] to develop a simple model that allows one to find the effect of the internal charge mobility on the external potential distribution and hence, on the electrostatic interaction between two approaching colloidal spheres. The internal charge redistribution manifests itself as a reduction of the electrostatic repulsion (or alternatively can be defined as an apparent additional attractive contribution to the energy see the inset in Fig. 3.9). While one may think that this is interaction is similar to the van der Waals attraction, the truth is that it has a very different functional dependence on separation. Instead of following a power law it decays almost exponentially, which is due to its electrostatic origin. It is very interesting that the effect of reduction in electrostatic repulsion is primarily dependent on the doping level and much less on whether the semiconductor particles are n-doped, p-doped or mixed. In addition to the n-doped particle interaction (the dashed line in Fig. 3.9) we have computed the interaction potentials between p-doped particles as well as that between an n-doped and a p-doped particle. All these curves practically collapse onto a single one, which is almost indistinguishable from the dashed curve in Fig. 3.9. This means that the main reason for the observed effect is that there is a dynamically responsive charged fluid in the particle interior that responds to potential perturbations. The polarity of the inner charges is practically unimportant.

The surface chemistry plays a key role in determining the strength of the interaction between semiconductor dopants and the electric double layer. The difference between the chemical equilibria constants $\Delta p\mathrm{K} = p\mathrm{K}_- - p\mathrm{K}_+$ determines the strength of the charge regulation at the interface [99]. Large $\Delta p\mathrm{K}$ allow for larger changes in the surface potential as the distance h is varied. Particle surfaces with low $\Delta p\mathrm{K}$ would show little change in stability with doping, while surfaces with large $\Delta p\mathrm{K}$ (i.e. silica, $\Delta p\mathrm{K} = 8$) allow for relatively large changes in surface potential and hence exhibit large changes in stability due to doping.

The new type of interaction, we have identified, has significant implications on the processing and handling of semiconductor colloids. First obvious conclusion is that doped colloids will be less stable and much more prone to coagulation than their undoped counterparts. Fig. 3.10 gives an idea about the relative time windows for kinetic stability. As mentioned above, the average lifetime for a suspension of silicon colloid with $10^{18}/\mathrm{cm}^3$ doping level will be more than 60 times shorter than that for an undoped sample with the same surface chemistry. This effect can be exploited to separate doped from undoped particles in aqueous suspensions, or even sort the particles based on their doping. Heavily doped particles will precipitate faster and can be separated from the rest by simple filtration or centrifugation. They then can be redispersed using sonication. The procedure can be repeated multiple times to obtain particles with narrow distribution of the doping levels.

Increasing the pH beyond the isoelectric point leads to an increase in the value of the surface potential and hence, increase the repulsion and stability of the suspension. Similar will be the effect of reducing the background electrolyte concentration, which will extend the range of the overall electrostatic repulsion. Colloidal suspensions can be used to fabricate ordered crystal-like structures that have excellent properties for photonics applications [120]. Fig. 3.9 implies that among other things the particle doping may have an effect on the spacing and ordering in crystals composed of

semiconductor colloidal particles. Doped particles will be spaced on the average closer than undoped particles. For example a close inspection of the energy curves in Fig. 3.9 show that the average doped particles spacing will be about 2 nm smaller than that for the undoped. We are convinced that better understanding of the interface between semiconductor materials and electrolyte solutions will be instrumental in the effort to design novel "smart" materials at the micro and nanoscale.

Chapter 4

Charge Regulating Density Functional Theory of Electric Double Layers

The physically correct and thermodynamically consistent representation of the charge at the surface of an electric double layer is given by the chemical equilibrium between the groups attached at the interface and the potential determining ions in the solution (i.e., charge regulation). Models that account for finite size effects of neutral solvent molecules are known as "civilized" models, while those that only account for finite size of ions are known as "primitive", and models that do not account for any finite size effects are called continuum models. In this chapter, we report that surface chemical equilibrium is strongly coupled to the precise molecular structure of the solution near the charged interface when using a "civilized" model. Therefore, all approaches that ignore the solvent structure such as continuum models based on the Poisson–Boltzmann equation or the "primitive" statistical mechanical models are at best only qualitatively correct and miss a range of important physical effects. Our analysis uses classical density functional theory to obtain the molecular and

ionic structure of an electric double with surface charge regulation and accounts for the contribution of the solvent. Our model suggests that the excluded volume of the solvent is the primary factor that couples the solution structure to the surface chemistry.

It is well known that the use of a continuum models to describe the properties of EDLs suffer from severe shortcomings [13–17]. Continuum models do not take into account the fact that the solution and ions both have an exhibit structure governed by excluded volume and long range interactions. This can lead to an unphysically high ionic concentrations near the interface. A much better theoretical framework for studying the properties of EDLs is offered by statistical mechanics [34, 37, 39–41, 121, 122]. Even statistical mechanical models are often simplified by representing the solvent as structureless continuum and account explicitly only for the ionic species. Such models are defined as "primitive". In contrast, models that take into account the excluded volume and long-ranged interactions for all participating species including the solvent fall under the category of "civilized" models [41]. The "primitive" model for very dilute electrolyte solutions gives the same results as the continuum theory based the Poisson–Boltzmann equation Eq. (1.3). The reason for this equivalence is that for dilute solutions there are too few ions for long range interactions, and finite size effects to significantly impact the solution.

The charge regulation condition has not been included in any statistical mechanical model until recently when Heinen et al. [39] incorporated it into a "primitive" model for charged colloidal suspension using the Ornstein–Zernike integral equation approach [32]. This work presents a major step forward but, as we show below, it is mostly qualitatively correct.

We argue that a physically correct description of an EDL should include charge regulation at the interface in conjunction with a "civilized" statistical mechanical model of the electrolyte solution. Such an analysis proves to be not just an in-

cremental improvement, but rather it offers a description that reveals a number of new effects, including possibilities for phase behaviors that all previous models have missed. The reason for that is that surface charge regulation [see Eqs. (1.8) and (1.10)] is extremely sensitive to the local structure and ionic density in the immediate vicinity of the reaction surface. While the most important species in that respect are the PDIs, their local density is dominated by the solvent structure due to its overwhelmingly high concentration. The effect of the solvent structure couples with the charge regulation surface chemical reactions given in Eq. (1.8) and strongly affects the resultant charge density. We demonstrate that the main factor leading to such a pronounced effect is the excluded volume of the solvent molecules. The long-ranged interactions, while still having an effect, are less important. Thus the coupling between structure and surface charge is driven by the partial entropy of the PDIs in the solution.

4.1 Theory

Our statistical mechanical analysis of the EDL is based on classical density functional theory (DFT) [34]. We start with the grand thermodynamic potential that has the form

$$\begin{aligned}\Omega[\{\rho_i\}] = F_{\rm id}\left[\{\rho_i\}\right] + F^{\rm ex}_{\rm HS}\left[\left\{\overline{\rho_i^{\rm HS}}\right\}\right] + F^{\rm ex}_{\rm long}\left[\left\{\overline{\rho_i^{\rm long}}\right\}\right] \\ + \sum_{i=1,N}\int d\mathbf{r}\rho_i(\mathbf{r})\left[V_i^{\rm ext}(\mathbf{r}) - \mu_i\right],\end{aligned} \tag{4.1}$$

where the ideal contribution to the free energy is given as

$$F_{\rm id}\left[\{\rho_i\}\right] = k_B T \sum_{i=1,N}\int d\mathbf{r}\rho_i(\mathbf{r})\left\{\ln\left[\Lambda_i^3\rho_i(\mathbf{r})\right] - 1\right\}, \tag{4.2}$$

$F^{\rm ex}_{\rm HS}\left[\left\{\overline{\rho_i^{\rm HS}}\right\}\right]$ is the contribution due to excluded volume (a hard sphere fluid of diameter $d_{\rm HS}$), and $F^{\rm ex}_{\rm long}\left[\left\{\overline{\rho_i^{\rm long}}\right\}\right]$ is the contribution due to long range interactions

(typically attractions). The appropriate hard sphere diameter can be determined using the Barker-Henderson criterion [56]. The quantity $\Lambda_i = \sqrt{h^2/(2\pi m_i k_B T)}$ is the thermal de Broglie wavelength, h is the Planck's constant, m_i is the mass of component "i", $\rho_i(\mathbf{r})$ and $\mu_i(\mathbf{r})$ are the local density variation and chemical potential of component "i" respectively, $V_i^{\text{ext}}(\text{r})$ is the external field and $\mathbf{r}$ is the coordinate normal to the interface. The interaction energy between species "i" and "j", Φ_{ij} includes both the electrostatic and Lennard-Jones attractions. It depends on the distance r_{ij} between molecules "i" and "j". The external field is due to the charge at the interface that essentially forms the EDL. The grand potential defined by Eq. (4.1) corresponds to an open system in contact with reservoirs for each species to ensure constant chemical potentials μ_i.

4.1.1 Formulation of Interactions

We consider an electrolyte dissolved in a solvent that exhibits both hard sphere and Lennard-Jones (LJ) interactions. The LJ contributions between two components in the electrolyte is given by

$$\Phi_{LJ}\left(r_{ij}\right) = \begin{cases} 4\epsilon_{ij}\left[\left(\frac{d_{ij}}{r_{ij}}\right)^{12} - \left(\frac{d_{ij}}{r_{ij}}\right)^{6}\right], & r_{ij} > d_{ij} \\ r_{\min}, & r_{ij} \leq d_{ij}, \end{cases} \tag{4.3}$$

while the LJ contributions between components of the electrolyte and wall is given by

$$\Phi_{LJ}\left(r_{ij}\right) = \begin{cases} \frac{2\pi}{3}\epsilon_{ij}\left[\frac{2}{15}\left(\frac{d_{ij}}{r_{ij}}\right)^{9} - \left(\frac{d_{ij}}{r_{ij}}\right)^{3}\right], & r_{ij} > d_{ij} \\ r_{\min}, & r_{ij} \leq d_{ij}, \end{cases} \tag{4.4}$$

where ϵ_{ij} is the magnitude of the LJ energy and d_{ij} is the distance between two particles where the potential reaches its minimum. All charged species, both in

solution and attached permanently at the EDL boundary also experience Coulombic interactions

$$\Phi_{el}\left(r_{ij}\right)=\frac{r_i z_j e^2}{4\pi\varepsilon\varepsilon_0 r_{ij}}, r_{ij}>d_{ij}. \tag{4.5}$$

If $r_{ij} < d_{ij}$, the interaction energy becomes infinite to account for the excluded molecular volume (i.e., finite size). The solution consists of (i) solvent molecules, (ii) PDIs (i.e., H_3O^+), (iii) background ions with the same charge as the PDIs that do not chemically bind to the EDL interface, and (iv) negative counterions that are common to the PDIs and background ions. This is a simplified model as it ignores the dipole molecular nature of polar solvents like water. Still it captures two very important physical characteristics of the solvent: the excluded volume of all species including the solvent and the attraction between all species (and the surface). Since the solvent is explicitly taken into account, this is a "civilized" model. The focus of the analysis is on the effect of the solvent structure and its coupling to the surface charge regulation mechanism in Eq. (1.8).

Following the general methodology of classical DFT, the grand potential given in Eq. (4.1) is then minimized with respect to the density distribution of each component in the solution. The minimization is accomplished using the Tramonto code [123,124]. We extend on Tramonto by adding charge regulating boundary conditions using a Python script described in Appendix F. This procedure gives the distribution of all the species in the solution. The surface charge σ_s is obtained by balancing it against the bulk excess charge to achieve global electro-neutrality.

4.1.2 Boundary Conditions

The application of charge regulating boundary conditions using DFT differs from application in previous chapters. In DFT, the natural quantities to work with are densities rather than potentials. For this reason we derive the charge regulating

boundary condition developed by Chan and Healy [21] given in Eq. (1.9) to be in terms of density so that

$$\sigma_s = e\Gamma \frac{\frac{[\mathrm{H_3O^+}]_s}{K_+} - \frac{K_-}{[\mathrm{H_3O^+}]_s}}{1 + \frac{[\mathrm{H_3O^+}]_s}{K_+} + \frac{K_-}{[\mathrm{H_3O^+}]_s}} = e\left(\frac{[\mathrm{H_3O^+}]_s}{K_+} - \frac{K_-}{[\mathrm{H_3O^+}]_s}\right) \tag{4.6}$$

where $[\mathrm{H_3O^+}]_s$ is the surface density of hydronium ions. The derivation of Eq. (4.6) is given in Appendix E. The relationship between the concentration of hydronium ions at the surface and the density distribution of hydronium ions provided by DFT is not obvious. Perhaps the easiest way to relate the two is to set them equal. We call this condition a "hard" boundary, and it is defined as

$$[\mathrm{H_3O^+}]_s = \rho_{\mathrm{PDI}}(0), \tag{4.7}$$

where $\rho_{\mathrm{PDI}}(0)$ is the density distribution of hydronium ions taken at the interface. In the case where the PDI is treated as a particle with no size, this treatment is correct and is equivalent to using the potential at the interface in the manner we use with the Poisson–Boltzmann equation in previous chapters. The situation when using DFT is more complicated because the components of the solvent have finite size, and when they react with the surface they retain aspects of their size. If we use the "hard" boundary condition, for similarly charge surfaces the contact density of the PDI will always be larger than the results obtained from a continuum model as shown in Fig. 4.1. Because of these dramatic increases in the density distribution near the interface, it is not clear that the concept of concentration used in chemical equilibria and the density distribution obtained by DFT are in fact the same quantities.

We propose a solution to this problem by using "soft" boundary conditions. By integrating the density distribution obtained by DFT near the interface over a particle radius we arrive at a quantity that is more representative of the concentration used in chemical equilibria. Here

$$[\mathrm{H_3O^+}]_s = \frac{\int_0^{d_{\mathrm{PDI}}/2} dz \rho_{\mathrm{PDI}}(z) w(z)}{\int_0^{d_{\mathrm{PDI}}/2} dz w(z)}, \tag{4.8}$$

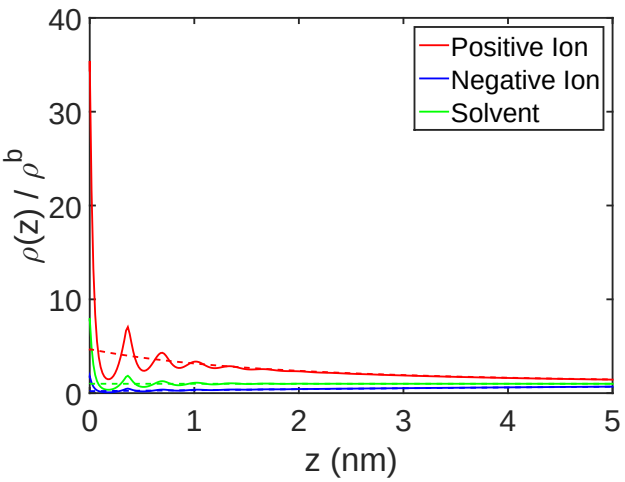

Fig. 4.1: Normalized density distributions using DFT (solid) and Poisson-Boltzmann (dashed) with the same surface charge density. While these two systems have the same surface charge density, the contact value $z = 0$ for the normalized densities are quite different with DFT giving a much larger value for all species.

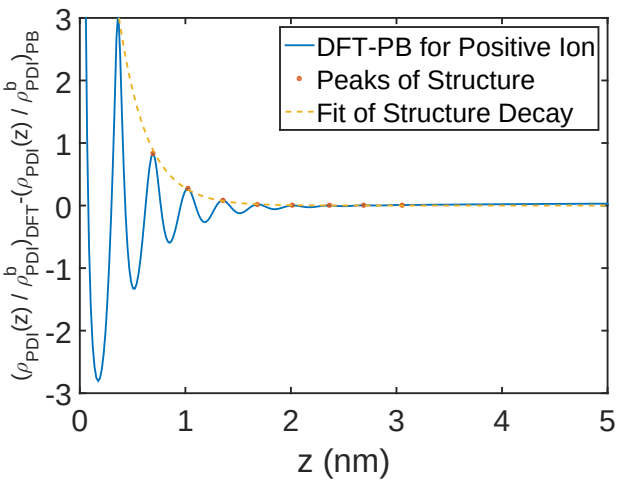

Fig. 4.2: Illustration of the effect of structure on the density distribution using DFT subtracted from the density distribution using Poisson-Boltzmann (blue). The peaks (red dots) of the effect of structure are fitted with an exponential (yellow dashed) to illustrate the structure decay length.

where $w(z)$ is a weighting factor. The factor $w(z)$ is introduced to account for the fact that the density distribution of a species at the interface is not equivalent to the surface concentration of a species when finite size effects are present. We expect that the expression for $w(z)$ is quite complicated, and at this point is unknown because it depends on the nature of the reaction mechanisms at the surface. Ideally we would obtain $w(z)$ using details from the particular reaction mechanism of interest, but for this work we assume a uniformly distributed $w(z) = 2/d_{\text{PDI}}$. This weighting is chosen primarily out of convenience and because it integrates to one. Is should be noted that Eq. (4.8) is equivalent to Eq. (4.7) as $d_{\text{PDI}} \to 0$ which provides consistency so that the "hard" and "soft" boundary conditions are equivalent in the limit where the solvent size is zero.

When using DFT and taking account for finite size effects of ions, there are two length scales of importance. The first is the Debye screening length κ^{-1} which is of key importance even in continuum models. The second length scale is strongly related to the size of the solvent and is illustrated in Fig. 4.2. By fitting an exponential $\alpha \exp(-\beta z)$ to the peaks of the structure, we arrive at a value of the structure decay length $\beta^{-1} = 3.78$ Å [125]. In the limit of a solid, β^{-1} goes to infinity, for a gas, β^{-1} tends towards zero but for a liquid β^{-1} has a finite value that depends on the liquid density and intermolecular interactions.

DFT and Molecular Dynamics provide very similar results in the domain of temperature and densities we consider for this dissertation and these similarities are illustrated in Fig. 4.3. The attractive interactions are controlled so that $\epsilon = \epsilon_{ij}$ is equal for all solvent-solvent interactions. In addition the solvent-wall attractive interactions are the same so that $\epsilon = \epsilon_{iw}$. As ϵ goes to 0, there are no attractions and the system becomes a hard sphere fluid at a hard wall.

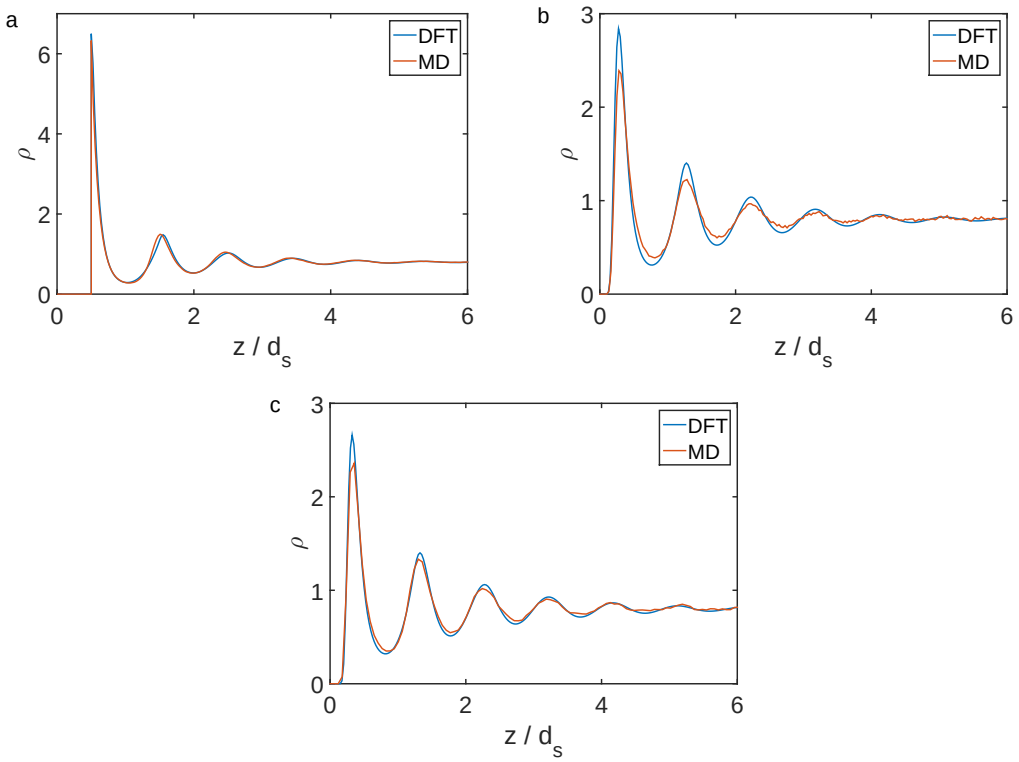

Fig. 4.3: Comparison between DFT and Molecular Dynamics results. It can be seen that the density profiles for a hard-sphere solvent with diameter d_s and Lennard-Jones interactions with (a) $\epsilon = 0.0\ k_BT$, (b) $\epsilon = 0.5\ k_BT$, and (c) $\epsilon = 1.0\ k_BT$ are all very close to each other demonstrating that DFT and Molecular Dynamics will give nearly the same results for the domain of interest in this dissertation. The DFT results shown here were all generated with the choice of hard sphere diameters $d_{\text{HS}} = d_{ij}$.

4.2 Results

The dependence of the surface charge σ_s on the size of the neutral solvent molecules is demonstrated in Fig. 4.4. using the "hard" boundaries in Fig. 4.4(a) and "soft" boundaries in Fig. 4.4(b). All other species have the same molecular diameter equal to 2.88 Å which is very close to experimentally measured values for water, potassium ion, chlorine ion, and hydronium [126]. The neutral solvent molecular diameter d_s varies from 0.0288 Å to 2.88 Å. The value 0.0288 Å is close to zero and represents the

"primitive" model, we chose not to simulate zero solvent size in order to avoid numerical problems. The value of 2.88 Å was selected to ensure total solution molarity of 55.6 M (molarity of water at standard temperature and pressure) for dimensionless density $\rho d_s^3 = 0.8$ characteristic of a liquid [127].

The LJ parameters for both the (9-13), and (6-12) potentials are assumed to be the same for all species so that $\epsilon_{_{LJ}} = \epsilon_{ij}$ for all combinations of interactions between components i and j. We then vary $\epsilon_{_{LJ}}$ from 0.0 k_BT and 0.5 k_BT. The ionic concentration is 10 mM which includes both PDIs and non-PDIs. Concentrations of the PDI and positively charge salt ion are adjusted for a particular pH so that bulk charge neutrality is satisfied. Each point in Fig. 4.4 is determined independently by running Tramonto starting from a uniform density distribution.

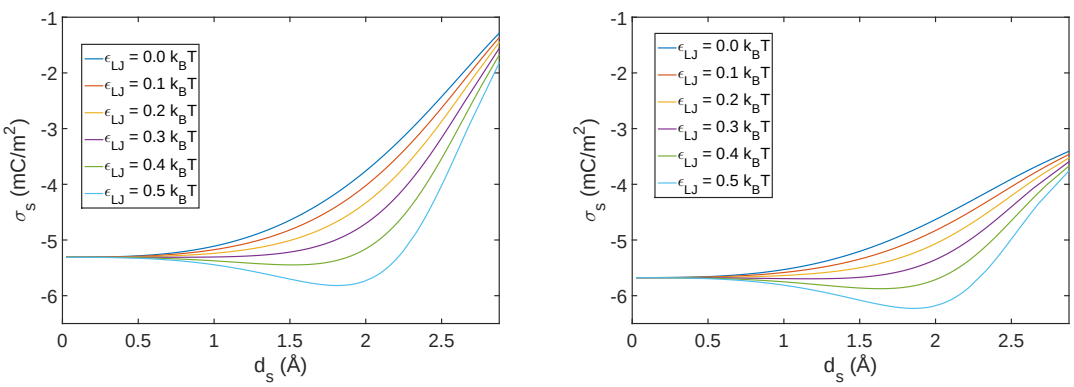

Fig. 4.4: Surface charge of an EDL as a function of the solvent molecular diameter. The different curves are for different values of the LJ parameter $\epsilon_{_{LJ}}$. Markers on each line represent points where simulations successfully ran, there are several locations in both plots where we were unable to obtain results, either due to numerical instabilities, or due to prohibitively long compute times.

For solvent with nearly zero molecular size, our system corresponds closely to a "primitive" model. In addition, for such low electrolyte concentrations, the "primitive" statistical mechanical model closely resembles the continuum analysis based on the Poisson equation, Eq. (1.1). Of course zero solvent size is unphysical, and when

taken into account results in significant deviations demonstrating the inadequacy of both the "primitive" and continuum models as seen in Fig. 4.4. The top curves in Figs. 4.4(a) and (b) illustrates the effect of purely excluded volume interactions on the surface charge σ_s. It shows that the magnitude of the surface charge rapidly changes after the solvent diameter exceeds $\sim$0.5 Å. The effect is very dramatic if when one realizes that the physically realistic case is when $d_s = 2.88$ Å, or the right edge of the figure. This is the size that corresponds to the density and overall molecular packing of a liquid state. This strong solvent effect on the surface charge is driven by the entropy changes in the bulk solution. As the solvent size increases, all ions (including the PDIs) have less free space, therefore their entropy decreases. Hence, they will be forced towards the surface, where they will chemically bind.

The attractive interactions facilitate the removal of the PDIs from the surface in order to be in closer contact with the solvent molecules. As attractive interactions increase, the pressure at the interface goes down according to the sum rule $p/k_BT = \sum_i \rho_i(0)$ where p is the pressure. The larger the parameter ϵ_{LJ}, the stronger the effect. However, it must be stressed that for molecular packing densities corresponding to a liquid solution again the far right limit of the plots are relevant and there the excluded volume dominates and the surface charge magnitude decreases. Still, there are detectable differences between cases with different attractive energies.

Again one concludes that any model that ignores the explicit structure of the solvent is missing an entire range of physical effects and will results in a quantitatively incorrect result for the surface charge density σ_s. Other quantities that depend on the surface charge such as electrostatic interactions and electrokinetic properties will be incorrect as well.

The difference between the "hard" and soft boundaries can be seen by comparing Figs. 4.4(a) and (b). For all sizes of the neutral solvent d_s the magnitude of the surface charge density σ_s is increased when using the "soft" boundaries. This effect

which results in an increase in surface charge is more dramatic in the liquid phase (where finite size effects are strong) than in the gas phase. The increase in charge density is a result of the soft boundaries averaging the density distribution near the interface.

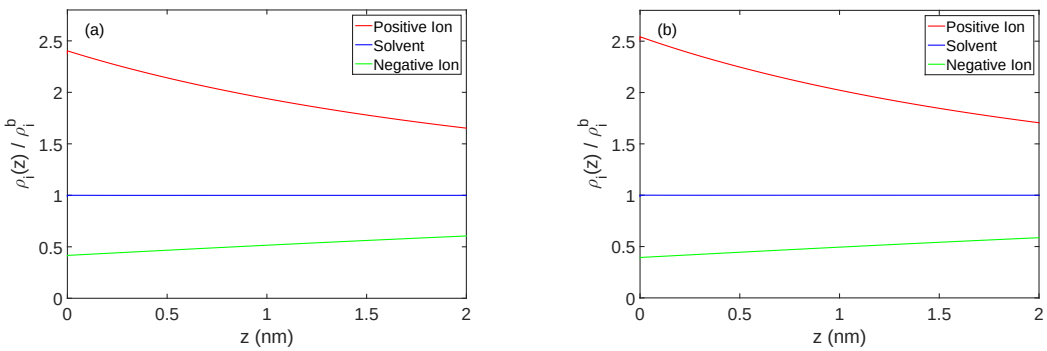

Fig. 4.5: Solution structure in terms of density distribution functions in the vicinity of the charged surface. Molecular diameter of solvent is $d_s = 0.0288$ Å Although calculated using DFT, this represents the "primitive" model limit where d_s is close to zero. (a) Hard boundary conditions using Eq. (4.7). There is no discernable structure for the neutral solvent while the positive and negative ions follow distributions identical to the modified Poisson–Boltzmann limit. (b) Soft boundary conditions using Eq. (4.8). Notice that the surface charge obtained using the soft boundary conditions is higher than using the hard boundary conditions.

The distribution of ions in the EDL for the "primitive" model using the hard and soft boundaries are shown in Figs. 4.5(a) and (b) respectively. Note that for such low concentration of ions, it practically coincides with the continuum model. The PDI and positive ion have identical normalized bulk density profiles so they are not plotted separately. Since this model is in the domain of the "primitive" model, the neutral solvent species maintains a uniform density distribution at its bulk density. The difference between hard and soft boundaries results in a slight increase in charge density at the surface as seen from the slightly higher density of positive ions, and slightly lower density of negative ions in Fig. 4.5(b). The reason the soft boundaries have lager surface densities at the surface is a result of the finite size of the PDI given in Eq. 4.8.

By increasing the size of the neutral solvent species to $d_s = 2.3$ Å and maintaining the total molarity of the solution at 55.6 M we begin to see finite size effects on charge regulation in Fig. 4.6. In *both* the cases where the hard boundary condition is used in Fig. 4.6(a), and where the soft boundary condition is used in Fig. 4.6(b) we see a decrease in the magnitude of the surface charge density. Near the interface, finite size effects are strong and result in structuring of the fluid. At distances larger than 1 nm the structural effects have decayed and the system behaves very much like the continuum model, the decay length of the structure is primarily determined by the volume fraction of the neutral solvent where increased volume fraction leads to longer structural decay lengths. The effect of structure increases the concentration of both the positive and negative ion at the interface beyond that which would be seen using the continuum model for the same surface charge density. The effect of van der Waals attractions within the solvent is an increase in the magnitude of the surface charge density when using either the hard or soft EDL boundaries. Attractions between the solvent and the PDI pull the PDI off the charged surface leading to an increased negative surface charge. The value $\rho d_s^3 = 0.41$ coupled with the similarities between the density profiles for $\epsilon_{\text{LJ}} = 0.0\ k_BT$ and $\epsilon_{\text{LJ}} = 0.4\ k_BT$ indicate that 0.4 k_BT is above the critical temperature.

At a neutral solvent size of $d_s = 2.88$ Å, again maintaining the total molarity of the solution at 55.6 M we achieve a dimensionless density $\rho d_s^3 = 0.8$ that is characteristic of a dense liquid. Fig. 4.7 illustrates density variations of a liquid at a charge regulating interface. Hard boundary conditions were used in Fig. 4.7(a) while soft boundary conditions were used in Fig. 4.7(b). In the liquid state, the effects of structure are quite clear. When Fig. 4.7 is compared to the two previous figures Figs. 4.6 and 4.5 it can be seen that in the liquid phase the effect of structure is the dominant contribution to the density profile, other effects such as those due to Debye screening are relatively minor (at the distances shown in the figures and for the pH and ionic strength chosen). Additionally, the effect of the van der Waals

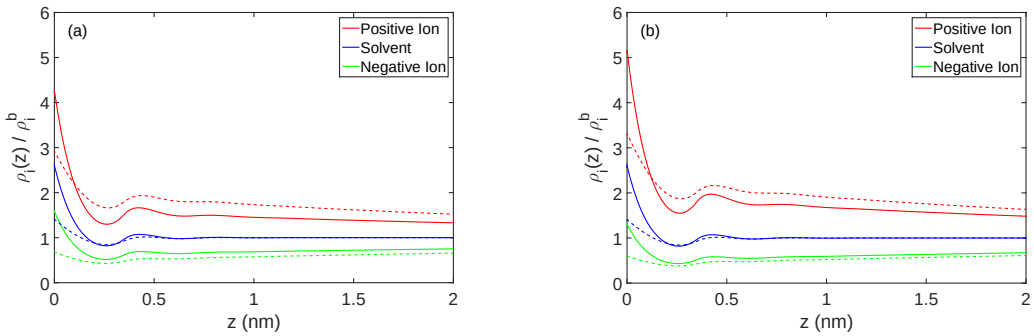

Fig. 4.6: Solution structure in terms of density distribution functions in the vicinity of the charged surface. Solid lines correspond to $\epsilon_{\text{LJ}} = 0.0\ k_BT$, dashed lines correspond to $\epsilon_{\text{LJ}} = 0.4\ k_BT$ Molecular diameter of solvent is $d_s = 2.3$ Å for a dimensionless density of $\rho d_s^3 = 0.41$ which corresponds to a supercritical fluid. (a) Hard boundary conditions using Eq. (4.7). (b) Soft boundary conditions using Eq. (4.8). Notice that the surface charge obtained using the soft boundary conditions is higher than using the hard boundary conditions.

attractions can also be seen to be comparatively small. The difference however between the hard and soft boundary conditions is significant, as in the previous two figures the soft boundary again has a larger surface charge density. Although the hard boundary conditions are easier to implement and are a natural extension from the boundary conditions used in the Poisson–Boltzmann continuum model, the soft boundary conditions are physically more realistic since they generalize the charge regulating boundary condition to account for finite size effects.

4.3 Conclusion

We have demonstrated that solvent structure has a significant effect on charge regulation. Together solvent size, structure and surface chemical equilibria couple to determine the surface charge. The primary reason for this coupling is due to the effect of excluded volume and solvent-ion attractions imposing structure on the ions

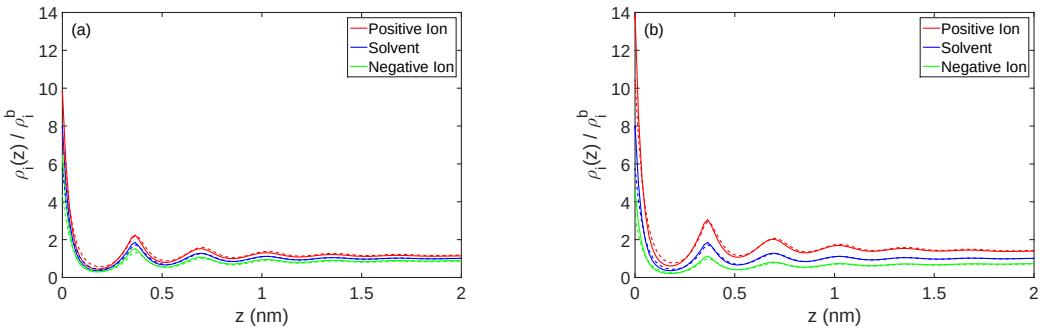

Fig. 4.7: Plots of solution structure in terms of density distribution functions in the vicinity of the charged surface. Solid lines correspond to $\epsilon_{\text{LJ}} = 0.0\ k_B T$, dashed lines correspond to $\epsilon_{\text{LJ}} = 0.4\ k_B T$ Molecular diameter of solvent is $d_s = 2.88$ Å for a dimensionless density $\rho d_s^3 = 0.8$. (a) Hard boundary conditions using Eq. (4.7). (b) Soft boundary conditions using Eq. (4.8). Notice that the surface charge obtained using the soft boundary conditions is higher than using the hard boundary conditions.

in solution.

Due to the low ionic concentrations ($\rho_{\text{ion}}/\rho_w < 0.02$ for 1 M and less) typically found in electrolyte the average ionic density distribution is dilute in bulk fluids, and for this reason "primitive" models offer little improvement over the continuum models like Poisson–Boltzmann. The overwhelmingly large concentration of neutral solvent relative to ions imposes structure on the ions that is determined by the finite size of the neutral solvent.

Continuum approaches based on the Poisson–Boltzmann equation and "primitive" statistical mechanical models describe gas phase systems. We have demonstrated that structural effects of the dense liquid phase have a significant effect on determining surface charge and therefore a "civilized" model is necessary to provide a quantitative description of charge regulation of the EDL.

Our model suggests several improvements for the future that are beyond the scope of this work. These improvements include the introduction of dipole moments for the solvent (to more closely mimic water molecules), and distinguishing between similarly

charged ions (such as Na^+ and K^+) through manipulation of the LJ interaction parameter ϵ_{LJ}. We are also of the opinion that improvements to the determination of $w(z)$ are necessary for a fully self consistent model.

Chapter 5

Summary and Conclusions

We have shown that charge regulation plays a fundamental role in determining the properties of fluidic nanoscale systems. Using charge regulating boundary conditions make three major conclusions.

We have determined that surface chemistry at the walls of fluidic nanochannels is critical to understanding transport of ionic species under the action of externally applied electric field. Charge regulation leads to a buffering effect that maintains the surface charge of a fluidic nanochannel relatively constant between the isoelectric point of the surface and $p\mathrm{H}_b = 7$. We also show that the complex combination of surface chemistry and ionic mobilities sometimes leads to counterintuitive drops in the local conductivity even if the overall electrolyte concentration is going up. These drops take place near the isoelectric point of the surface and around $p\mathrm{H}_b = 7$. In the first case this is attributed to the different mobilities of the present positive and negative ions, while the latter is due to the mobility differences between the potential determining and indifferent counterions.

A new type of interaction is identified that has significant implications on the processing and handling of semiconductor colloids. We conclude that that doped

colloids will be less stable and much more prone to coagulation than their undoped counterparts. This difference in stability may result in more than 60 times shorter coagulation times for doped colloids than that for an undoped sample with the same surface chemistry. This effect may be exploited to separate doped from undoped particles in aqueous suspensions, or even sort the particles based on their doping.

We also demonstrate that solvent structure has a profound effect on surface charge densities and in general results in structuring the potential determining ions near the interface. The effect of structure demonstrates that the continuum models such as Poisson–Boltzmann, and "primitive" models that are fundamentally gas phase are insufficient to quantitatively describe charge regulation of an EDL and that a "civilized" models is necessary to adequately account for the structural impact on ions due to the presence of neutral solvent molecules.

A great deal of future work remains. This will include experimental verification of the predictions of nanochannel conductivity through voltage measurements of nanochannels near their isoelectric points. It is possible that the predictions regarding stability of semiconductor colloids will have processing applications for separation of doped and undoped species and self-assembly. Further, we expect improvements on charge regulating DFT can be made by extending the solvent model to include dipole moments and hydrogen bonding. Perhaps the area that promises the most improvement is in finding better choices for the weighting factor $w(z)$. We are confident these improvements will bring us closer to a truly quantitative and predictive model of the electrostatic double-layer.

Appendix A

Calculations of energy of interaction between colloidal particles

Obtaining energy of interaction between two spherical semiconductor colloidal particles suspended in aqueous electrolyte solution. Knowing the relationship between charge density and potential allows us to obtain the electrostatic disjoining pressure Π_e between two flat bodies separated by a layer of electrolyte of thickness h

$$\Pi_e(h) = 2Nk_BT\left[\cosh\left(e\Psi_m/k_BT\right) - 1\right], \tag{A.1}$$

where Ψ_m is the potential in the midplane between the surfaces. The dependence of the disjoining pressure on the separation between the flat surfaces follows from the fact that both the electrostatic potential and the charge density depend on h. Integrating the pressure the separation gives the electrostatic energy per unit area

$$f_i(h) = \int_h^\infty dz\Pi_e(z), \tag{A.2}$$

which allows obtaining the pair electrostatic energy of interaction between two spherical microparticles of radius a,

$$U_e(h) = \pi a \int_h^\infty dz f_e(z). \tag{A.3}$$

When doing the integrations over the distances one should bear in mind that the surface potential Ψ_s and charge σ_s depend on the separation. The total energy of interactions is a superposition of the electrostatic contribution and the van der Waals attractive energy

$$U_{\text{vdw}}(h) = -\frac{A_H a}{12h}, \tag{A.4}$$

where A_H is the Hamaker constant. The total energy of interaction is then given by

$$U(h) = U_e(h) + U_{\text{vdw}}(h). \tag{A.5}$$

The coagulation kinetics of colloid dispersions usually follows a diffusion controlled mechanism as first outlined by Smoluchowski [114] for the case of absence of any long-range interactions. It was later extended to included the effects of energy barriers by Fuchs [116] and Debye [115]. According to the theory of diffusion controlled reactions the kinetic constant for coagulation of two particles is given by

$$k_c = \frac{k_0}{W}, \tag{A.6}$$

where k_0 is the rate constant of barrierless (unobstructed by repulsive forces) coagulation. The effect of the interaction energy is accounted for by the stability factor

$$W = 4a \int_0^\infty dh \frac{H(h) \exp[U(h)/k_B T]}{h - 2a}. \tag{A.7}$$

The function

$$H(h) = \frac{D_0}{D(h)}, \tag{A.8}$$

takes into account the hydrodynamic interactions between the particles, which generally depend on the distance between the particles surfaces [117]. The diffusion coefficient $D(h)$ accounts for the effect on close field hydrodynamics that determines the behaviour at close separation. We will express it through the interpolating function

$$D(h) = \frac{D_0 D_T(h)}{D_0 + D_T(h)}, \tag{A.9}$$

where D_0 and $D_T(h)$ are are the Stokes-Einstein and the diffusion coefficient that accounts for small distance Taylor type hydrodynamic interactions [112]

$$D_0 = \frac{k_B T}{6\pi\eta a}, \quad D_T = \frac{2k_B T h}{3\pi\eta a^2}. \tag{A.10}$$

The integral in Eq. (A.7) can be approximated using the Laplace method according to which

$$\int_0^\infty dh \frac{H(h)\exp\left[U(h)/k_B T\right]}{h-2a} \approx \sqrt{\frac{2\pi k_B T}{|U''(h_m)|}} \frac{H(h_m)}{h_m - 2a} \exp\left[U(h_m)/k_B T\right]. \tag{A.11}$$

The distance h_m corresponds to the maximum of the function $U(h)$, which is the top of the energy barrier. The pre-exponential factor in Eq. (A.11) is almost the same for doped and undoped particles. Hence the main difference in the coagulation kinetics will be determined by the ratio

$$\frac{(k_c)_{\text{doped}}}{(k_c)_{\text{undoped}}} = \frac{W_{\text{undoped}}}{W_{\text{doped}}} = \exp\left(\frac{\Delta U}{k_B T}\right). \tag{A.12}$$

Appendix B

Linearization of the surface potential subject to charge regulation

Linearization of Eqs. (1.1) and (3.3) in the text, subject to the boundary conditions given in Eqs. (3.7), (3.8) and (1.10) results in an expression for the surface potential, the tilde above the variable denotes a dimensionless variable so that $\widetilde{\Psi} = e\Psi/k_BT$,

$$\widetilde{\Psi}_{\mathrm{el}} = \widetilde{\Psi}_s \frac{\cosh[\kappa_{\mathrm{el}}(x - L_{\mathrm{el}}/2)]}{\cosh(\kappa_{\mathrm{el}} L_{\mathrm{el}}/2)} \tag{B.1}$$

$$\widetilde{\Psi}_{\mathrm{ox}}(x) = \widetilde{\Psi}_s + \frac{\widetilde{\Psi}_s - \widetilde{\Psi}_q}{L_{\mathrm{ox}}} x \tag{B.2}$$

$$\widetilde{\Psi}_{\mathrm{sc}}(x) = \widetilde{\Psi}_q \exp[\kappa_{\mathrm{sc}}(x + L_{\mathrm{ox}})] \tag{B.3}$$

we define Ψ_q as the potential at the semiconductor-oxide interface as a matter of convenience. Charge regulating boundary condition at the oxide-electrolyte interface is given as,

$$\sigma_s = \mathbf{n} \cdot \left(\varepsilon_{\mathrm{ox}} \varepsilon_0 \left. \frac{d\Psi_{\mathrm{ox}}}{dx} \right|_{x=0} - \varepsilon_{\mathrm{el}} \varepsilon_0 \left. \frac{d\Psi_{\mathrm{el}}}{dx} \right|_{x=0} \right). \tag{B.4}$$

Substituting the values of the derivatives we get,

$$\sigma_s = \mathbf{n} \cdot \left[\varepsilon_{\text{ox}} \varepsilon_0 \frac{\Psi_s - \Psi_q}{L_{\text{ox}}} + \varepsilon_{\text{el}} \varepsilon_0 \Psi_s \kappa_{\text{el}} \tanh\left(\frac{\kappa_{\text{el}} L_{\text{el}}}{2} \right) \right]. \tag{B.5}$$

If we linearize the surface charge σ_s for small $\widetilde{\Psi}_s \ll 1$ we arrive at

$$\sigma_s = e\Gamma \frac{\delta \sinh\left(\widetilde{\Psi}_N - \widetilde{\Psi}_s\right)}{1 + \delta \cosh\left(\widetilde{\Psi}_N - \widetilde{\Psi}_s\right)} \approx \frac{e\Gamma\delta \sinh\left(\widetilde{\Psi}_N\right)}{1 + \delta \cosh\left(\widetilde{\Psi}_N\right)} - \frac{e\Gamma\delta\left[\delta + \cosh\left(\widetilde{\Psi}_N\right)\right]}{\left[1 + \delta \cosh\left(\widetilde{\Psi}_N\right)\right]^2} \tag{B.6}$$

and

$$\frac{e\Gamma\delta \sinh\left(\widetilde{\Psi}_N\right)}{1 + \delta \cosh\left(\widetilde{\Psi}_N\right)} - \frac{e\Gamma\delta\left[\delta + \cosh\left(\widetilde{\Psi}_N\right)\right]}{\left[1 + \delta \cosh\left(\widetilde{\Psi}_N\right)\right]^2} \widetilde{\Psi}_s = \tag{B.7}$$

$$\mathbf{n} \cdot \left[\varepsilon_{\text{ox}} \varepsilon_0 \frac{\widetilde{\Psi}_s - \widetilde{\Psi}_q}{L_{\text{ox}}} + \varepsilon_{\text{el}} \varepsilon_0 \widetilde{\Psi}_s \kappa_{\text{el}} \tanh\left(\frac{\kappa_{\text{el}} L_{\text{el}}}{2} \right) \right]$$

The boundary conditions at the semiconductor-oxide interface are

$$\varepsilon_{\text{sc}} \varepsilon_0 \widetilde{\Psi}_q \kappa_{\text{sc}} = \varepsilon_{\text{ox}} \varepsilon_0 \frac{\widetilde{\Psi}_s - \widetilde{\Psi}_q}{L_{\text{ox}}} \tag{B.8}$$

and

$$0 = \mathbf{n} \cdot \left(\varepsilon_{\text{sc}} \varepsilon_0 \left. \frac{d\Psi_{\text{sc}}}{dx} \right|_{x=-L_{\text{ox}}} - \varepsilon_{\text{ox}} \varepsilon_0 \left. \frac{d\Psi_{\text{ox}}}{dx} \right|_{x=-L_{\text{ox}}} \right) \tag{B.9}$$

or

$$\widetilde{\Psi}_q = \frac{\varepsilon_{\text{ox}} \widetilde{\Psi}_s}{L_{\text{ox}} \varepsilon_{\text{sc}} \kappa_{\text{sc}} + \varepsilon_{\text{ox}}} \tag{B.10}$$

and

$$\frac{e\Gamma\delta \sinh\left(\widetilde{\Psi}_N\right)}{1 + \delta \cosh\left(\widetilde{\Psi}_N\right)} - \frac{e\Gamma\delta\left[\delta + \cosh\left(\widetilde{\Psi}_N\right)\right]}{\left[1 + \delta \cosh\left(\widetilde{\Psi}_N\right)\right]^2} \widetilde{\Psi}_s = \tag{B.11}$$

$$\varepsilon_{\text{ox}} \varepsilon_0 \frac{\widetilde{\Psi} - \frac{\varepsilon_{\text{ox}} \widetilde{\Psi}_s}{L_{\text{ox}} \varepsilon_{\text{sc}} \kappa_{\text{sc}} + \varepsilon_{\text{ox}}}}{L_{\text{ox}}} + \varepsilon_{\text{el}} \varepsilon_0 \widetilde{\Psi}_s \kappa_{\text{el}} \tanh\left(\frac{\kappa_{\text{el}} L_{\text{el}}}{2} \right) \tag{B.12}$$

Solving for $\widetilde{\Psi}_s$ yields,

$$\widetilde{\Psi}_s = \frac{e\Gamma\delta\sinh\left(\widetilde{\Psi}_N\right)}{\left[\delta\cosh\left(\widetilde{\Psi}_N\right)+1\right]\left\{\varepsilon_0\varepsilon_{\rm el}\kappa_{\rm el}\tanh\left(\frac{\kappa_{\rm el}h}{2}\right)+\frac{\varepsilon_0\varepsilon_{\rm ox}\kappa_{\rm sc}}{\varepsilon_0+L_{\rm ox}\varepsilon_{\rm sc}\kappa_{\rm sc}}+\frac{e^2\Gamma\delta\left[\cosh\left(\widetilde{\Psi}_N\right)+\delta\right]}{k_BT\left[\delta\cosh\left(\widetilde{\Psi}_N\right)+1\right]^2}\right\}} \tag{B.13}$$

Note that for $L_{\rm ox}\to\infty$ (the limit of infinite oxide thickness) or $\kappa_{\rm sc}\to 0$ (undoped semiconductor) the system becomes identical to a dielectric-electrolyte interface

$$\widetilde{\Psi}_s = \frac{e\Gamma\delta\sinh\left(\widetilde{\Psi}_N\right)}{\left[\delta\cosh\left(\widetilde{\Psi}_N\right)+1\right]\left\{\varepsilon_0\varepsilon_{\rm el}\kappa_{\rm el}\tanh\left(\frac{\kappa_{\rm el}h}{2}\right)+\frac{e^2\Gamma\delta\left[\cosh\left(\widetilde{\Psi}_N\right)+\delta\right]}{k_BT\left[\delta\cosh\left(\widetilde{\Psi}_N\right)+1\right]^2}\right\}} \tag{B.14}$$

and for $L_{\rm ox}\to 0$ (the limit of negligible oxide thickness)

$$\widetilde{\Psi}_s = \frac{e\Gamma\delta\sinh\left(\widetilde{\Psi}_N\right)}{\left[\delta\cosh\left(\widetilde{\Psi}_N\right)+1\right]\left\{\varepsilon_0\varepsilon_{\rm el}\kappa_{\rm el}\tanh\left(\frac{\kappa_{\rm el}h}{2}\right)+\varepsilon_{\rm ox}\kappa_{\rm sc}+\frac{e^2\Gamma\delta\left[\cosh\left(\widetilde{\Psi}_N\right)+\delta\right]}{k_BT\left[\delta\cosh\left(\widetilde{\Psi}_N\right)+1\right]^2}\right\}} \tag{B.15}$$

where, $\kappa_{\rm el}$ and $\kappa_{\rm sc}$ are the inverse Debye lengths of the electrolyte and semiconductor regions respectively, and I is the ionic strength of the electrolyte, N_A is Avogadros number, and N_d is the total doping concentration of the semiconducting region. The screening parameters in the electrolyte and semiconductors phases are given by

$$\kappa_{\rm el}^{-1} = \sqrt{\frac{\varepsilon_{\rm el}\varepsilon_0 k_BT}{n_{\rm el}e^2}}, \tag{B.16}$$

and

$$\kappa_{\rm sc}^{-1} = \sqrt{\frac{\varepsilon_{\rm sc}\varepsilon_0 k_BT}{n_{\rm sc}e^2}}. \tag{B.17}$$

Note that for undoped semiconductor phase $\kappa_{\rm sc}$ and Eq. (B.15) becomes identical to the dielectric-electrolyte case [see Eq. (B.14)]. Since this linearization assumes that Ψ_s is small, it is only applicable for small (< 26 mV) surface potentials. The linearization provides a reasonable approximation to the full simulation when the

pH is close to the isoelectric point (in this case pI = 2). When the pH = 4, the difference in pH from the isoelectric point results in larger surface potentials, and hence less accuracy given by Eq. (B.14). A comparison between numerical and linearized analytical results is presented in Fig. B.1 below. The surface potential of two interacting charge regulating interfaces varies with the distance between them [20,21,108]. These variations, however, are different for doped and undoped particles as seen in the figure.

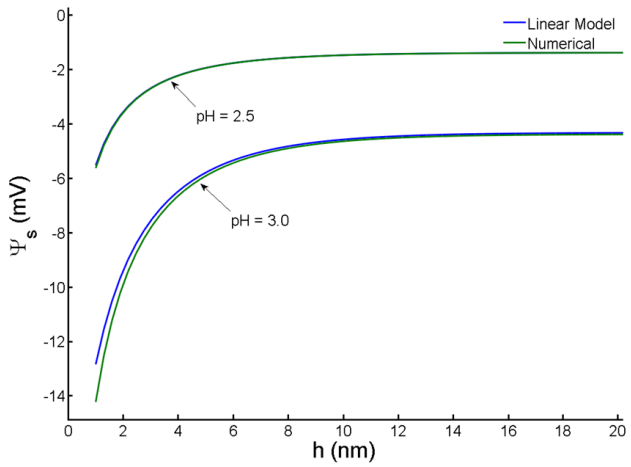

Fig. B.1: Surface potential for undoped and doped particles as a function of distance. Both numerical and analytical [see Eq. (B.13)] results are shown for comparison.

Appendix C

Charge Density Determined by the Fermi-Dirac Distribution

Our derivation below is for the particular case of n-doped semiconductor where the mobile charges are electrons, which is in contact with electrolyte solution across a thin oxide layer. The result for p-doped would be similar. The equation that we need to solve is

$$\frac{d^2\tilde{\Psi}}{d\tilde{x}^2} = -\left[1 - \chi F_{1/2}\left(\tilde{\mu} - \tilde{\Psi}\right)\right] \tag{C.1}$$

where we have adopted the notation $\tilde{\Psi} = e\Psi/\varepsilon_r\varepsilon_0 k_B T$, $\tilde{\mu} = \mu/k_B T$, and $\tilde{x}^2 = x^2 e^2 N_d/\varepsilon_r\varepsilon_0 k_B T$. The Eq. (C.1) is multiplied by $2(d^2\tilde{\Psi}/d\tilde{x}^2)$ and integrated. For a single electric double layer the potential and its derivative vanish far away from the interface and the results is

$$\frac{d\tilde{\Psi}}{d\tilde{x}} = \left\{2\chi\left[F_{3/2}\left(\tilde{\mu} - \tilde{\Psi}\right) - F_{3/2}\left(\tilde{\mu}\right)\right] - 2\tilde{\Psi}\right\}^{1/2} \tag{C.2}$$

where

$$F_{3/2}(x) = \frac{1}{\Gamma(5/2)}\int_0^\infty dt \frac{t^{3/2}}{1 + \exp(t - x)}, \tag{C.3}$$

is a Fermi integral of order 3/2. A second formal integration leads to

$$\int_{\tilde{\Psi}_0}^{\tilde{\Psi}} \frac{d\Psi}{\left\{2\chi\left[F_{3/2}\left(\tilde{\mu}-\tilde{\Psi}\right)-F_{3/2}\left(\tilde{\mu}\right)\right]-2\tilde{\Psi}\right\}^{1/2}} = \tilde{x}. \tag{C.4}$$

The surface potential $\tilde{\Psi}_0$ is defined at the semiconductor-oxide interface and has to be determined from the boundary conditions given in Eq. (3.7) and Eq. (3.8).

Appendix D

Fermi Level at a Semiconductor-Oxide-Electrolyte Interface

The value of the Fermi level (i.e., the chemical potential of the electrons) is necessary to know when the Boltzmann approximation given in Eq. (3.6) fails and the Fermi-Dirac distribution has to be used in the semiconductor with Eq. (3.3). The determination of the Fermi level depends on the system. If transfer of charge (in this case an electron) is allowed, the Fermi level in the semiconductor would be fixed through an appropriate boundary condition at the interface with the adjacent phase [128]. If electron transfer between the phases is not possible, the Fermi level can be obtained from the condition for charge conservation [110]. A particularly simple case is when the semiconductor phase is large enough so that the total charge due to donors and free electrons far away from the charged interface becomes zero. At this point the electrostatic potential will also vanish and the Fermi level can be

obtained through the charge neutrality condition

$$1 - \chi F_{1/2}\left(\frac{\mu}{k_B T}\right) = 0. \tag{D.1}$$

This is the equation we use to find the Fermi level for calculating the properties of a single semiconductor-oxide-electrolyte interface above. The value of μ depends only on the parameter χ [see Eq. (D.1)]. Fig. D.1 shows the dependence of the Fermi level on the parameter χ obtained by solving Eq. (D.1).

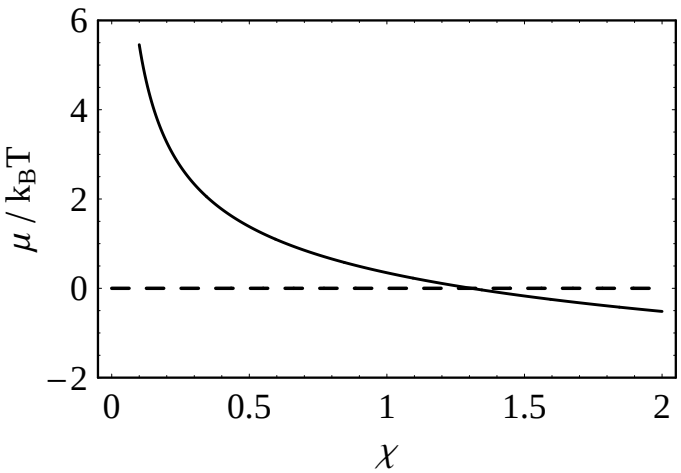

Fig. D.1: Fermi level μ vs the parameter χ.

Appendix E

Derivation of boundary conditions for density functional calculation

Using the chemical equilibria for amphoteric surfaces we have,

$$K_+ = \frac{[AH][\mathrm{H_3O^+}]_s}{[AH_2^+]}, K_- = \frac{[A^-][\mathrm{H_3O^+}]_s}{[AH]} \tag{E.1}$$

We rearrange in terms of $[AH]$,

$$[AH] = \frac{K_+[AH_2^+]}{[\mathrm{H_3O^+}]_s} = \frac{[A^-][\mathrm{H_3O^+}]_s}{K_-} \tag{E.2}$$

$$[AH_2^+] = \frac{[AH][\mathrm{H_3O^+}]_s}{K_+} \tag{E.3}$$

$$[A^-] = \frac{K_-[AH]}{[\mathrm{H_3O^+}]_s} \tag{E.4}$$

The boundary conditions given in terms of amphoteric groups is expressed as,

$$\sigma_s = e\Gamma \frac{[AH_2^+] - [A^-]}{[AH_2^+] + [AH] + [A^-]} \tag{E.5}$$

and by substitution we arrive at,

$$\sigma_s = e\Gamma \frac{\frac{[\mathrm{H_3O^+}]_s}{K_+} - \frac{K_-}{[\mathrm{H_3O^+}]_s}}{1 + \frac{[\mathrm{H_3O^+}]_s}{K_+} + \frac{K_-}{[\mathrm{H_3O^+}]_s}} = e\left(\frac{[\mathrm{H_3O^+}]_s}{K_+} - \frac{K_-}{[\mathrm{H_3O^+}]_s}\right) \tag{E.6}$$

Appendix F

Documentation of Python Interface for Running Tramonto

Tramonto [124] is software developed at Sandia National Laboratories that uses fluid density function theory (DFT) to compute fluid structure near surfaces. Tramonto is capable of natively solving DFT problems for interfacial problems in 1D, 2D, and 3D. For the work in this dissertation however, we use Tramonto only in 1D.

Tramonto supports both constant surface charge density boundary conditions, and constant surface potential boundary conditions. Neither of these boundary conditions are sufficient to solve a charge regulating problem in a single run. Since charge regulating boundary conditions are not supported in Tramonto, we offer a script that augments the capabilities of Tramonto to provide these boundary conditions. The script, `tramonto.py` contains a class that interfaces with the Tramonto code and runs it in parallel using `mpirun`. In order to run DFT charge regulating simulations, it is recommended that you interface with `tramonto.py` through the another script provided `sweep.py`, which at this time requires some rudimentary Python programming skills. The script `sweep.py` interfaces with `tramonto.py`, initializes the simulation,

runs and saves the simulation.

The routines provided in tramonto.py are provided below with a description of their functionality.

`readDFTInputFile(self, fileName):`
Reads the file, `fileName`, in almost every case this file will be `dft_input.main`. This file contains the default options that the user would like to run with Tramonto.

`getSurfaceDensities(self):`
This function reads the file `dft_dens.dat` and locates the first non-zero density entry. If it fails, it returns 0.

`calculateResidual(self, surfaceChargeDensity):`
Looks up the surface charge densities from the most recent run. Calculates the residual r as

$$r = \sigma_s - e\Gamma\delta \frac{\delta \sinh\left[\frac{e}{k_B T}\left(\Psi_N - \Psi_s\right)\right]}{1 + \delta\cosh\left[\frac{e}{k_B T}\left(\Psi_N - \Psi_s\right)\right]} \tag{F.1}$$

`constantCharge(self, surfaceCharge):`
Reads input file using `readDFTInputFile`, then creates a new input file that will be read directly by tramonto called, `dft_input.dat`. This function assumes that the contents of `dft_input.dat` have fixed line numbers for every option, if Tramonto is ever modified, this may change and could be broken in the next version. The file `dft_surfaces.dat` is also written to with the appropriate constant charge boundary conditions. Tramonto is then called using `mpirun`, and is run on 8 cores. The results of the run of Tramonto that are typically of interest will be stored in the file `dft_dens.dat`.

`plot(self, *arg):` This function was used to visualize output from Tramonto. It simply makes a call to `gnuplot` and visualized the density distributions. This

function is depreciated and is not recommended for use.

`chargeRegulation(self)`: Runs Tramonto repeatedly using constant charge density boundary conditions using a bisection method to arrive at the charge regulating boundary conditions. First Tramonto is run in the extreme charge densities of $\sigma_s \pm e\Gamma$. The residual is calculated using Eq. (F.1), and a bisection method is used to find the root of the residual. Once the root is found so that $r = 0$, charge regulating boundary conditions are satisfied.

`save(self, filename)`: This simply copies the file `dft_dens.dat` to a file named `[filename].density` and the temporary file `[filename].tmp` to `[filename].output`. This function is useful to save results when running multiple simulations as part of a single run.

References

[1] J. N. Israelachvili, Intermolecular and Surface Forces, 2nd Edition, Academic Press Limited, 1992.

[2] J. Fritz, E. B. Cooper, S. Gaudet, P. K. Sorge, S. R. Manalis, Electronic detection of dna by its intrinsic molecular charge, PNAS 110 (2010) 389–458.

[3] E. J. W. Verwey, J. T. G. Overbeek, Theory of the Stability of Lyophobic Colloids, Elsevier Publishing Company, Inc., 1948.

[4] H. Helmholtz, Ueber einige gesetze der vertheilung elektrischer strme in krperlichen leitern mit anwendung auf die thierisch-elektrischen versuche, Annalen der Physik und Chemie (in German) 165(6) (1853) 211–233.

[5] G. Gouy, Sur la constitution de la charge 'electrique 'a la surface d'un electrolyte, J. Physique 9 (1910) 457–468.

[6] D. L. Chapman, A contribution to theory of capillarity, Phil. Mag. 25 (1913) 475.

[7] H. Oshima, Theory of Colloid and Interfacial Electric Phenomena, Elsevier Ltd.

[8] L. B. Bhuiyan, C. W. Outhwaite, Comparison of the modified Poisson-Boltzmann theory with recent density functional theory and simulation results in the planar electric double layer, Phys. Chem. Chem. Phys. 6 (2004) 3467–3473.

[9] J. Wu, Density functional theory for chemical engineering: From capillarity to soft materials, AIChE Journal 52 (3) (2006) 1169–1191.

[10] D. Henderson (Ed.), Fundamentals of Inhomogeneous Fluids, Marcel Dekker, Inc., 1992.

[11] D. F. Evans, H. Wennerström, The Colloidal Domain, Wiley-VCH, 1999.

[12] O. Stern, Zur theorie der elektrolytischen doppelschicht, Z. Electrochem 30 (1924) 508–516.

[13] I. Borukhov, D. Andelman, Steric effects in electrolytes: A modified Poisson-Boltzmann equation, Phys. Rev. Lett. 79(3) (1997) 435–438.

[14] I. Borukhov, D. Andelman, D. A. H. Orland, Adsorption of large ions from an electrolyte solution: A modified poisson-boltzmann equation, Electrochim. Acta 46(2-3) (2000) 221–229.

[15] D. Ben-Yaakov, D. Andelman, D. Harries, R. Podgornik, Beyond standard poisson-boltzmann theory: Ion-specific interactions in aqueous solutions, J. Phys.: Condens. Matter 21 (2009) 424106.

[16] D. Ben-Yaakov, D. Andelman, R. Podgornik, D. Harries, Ion-specific hydration effects: Extending the poisson-boltzmann theory, Curr. Opin. Colloid and Interface Sci. 11 (2011) 542–550.

[17] P. M. Biesheuvel, M. v. d. Veen, W. Norde, A modified poisson-boltzmann model including charge regulation for the adsorption of ionizable polyelectrolytes to charged interfaces, applied to lysozyme adsorption on silica, J. Phys. Chem. B 109 (2005) 4172–4180.

[18] B. Derjaguin, L. Landau, Theory of the stability of strongly charged lyophobic sols and the adhesion of strongly charged particles in solution of electrolytes, Acta. Physicochim. URSS 14 (1941) 633–662.

[19] H. C. Hamaker, The london-van der waals attraction between spherical particles, Physica 4 (1937) 1058–1072.

[20] B. W. Ninham, V. A. Parsegian, Electrostatic potential between surface bearing ionizable groups in ionic equilibrium with physiologic saline solution, J. Theor. Biol. 31 (1971) 405–428.

[21] D. Y. C. Chan, T. W. Healy, L. R. White, Electrical double layer interactions under regulation by surface ionization equilibria–dissimilar amphoteric surfaces, J. Chem. Soc., Faraday Trans. I 72 (1976) 2844–2865.

[22] S. H. Behrens, M. Borkovec, Exact Poisson-Boltzmann solution for the interaction of dissimilar charge-regulating surfaces, Phys. Rev. E 60 (1999) 7040–7048.

[23] D. Y. C. Chan, T. W. Healy, T. Supasiti, S. Usui, Electrical double layer interactions between dissimilar oxide surfaces with charge regulation and stern–grahame layers, J. Colloid Interface Sci. 296 (2006) 150–158.

[24] S. H. Behrens, M. Borkovec, Electrostatic interaction of colloidal surfaces with variable charge, J. Phys. Chem. 103 (1999) 2918–2928.

[25] S. H. Behrens, D. G. Grier, The charge of glass and silica surfaces, J. Chem. Phys. 115 (2001) 6716–6721.

[26] J. G. Kirkwood, On the theory of strong electrolyte solutions, J. Chem. Phys. 2 (1934) 767–781.

[27] F. H. Stillinger, J. G. Kirkwood, Theory of the diffuse double layer, J. Chem. Phys. 33 (1960) 1282–1290.

[28] F. F. Buff, F. H. Sillinger, Statistical mechanical theory of doublelayer structure and properties, J. Chem. Phys. 39 (1963) 1911–1923.

[29] J. G. Kirkwood, Theory of Solutions, Gordon and Breach, 1968.

[30] E. Meeron, Theory of potentials of average force and radial distribution functions in ionic solutions, J. Chem. Phys. 28 (1958) 630–643.

[31] J. E. Mayer, The theory of ionic solutions, J. Chem. Phys. 18 (1950) 1426–1436.

[32] D. A. McQuarrie, Statistical Mechanics, Sausalito: University Science Books, 2000.

[33] R. Balescu, Equilibrium and non-equilibrium statistical mechanics, Wiley, 1975.

[34] L. Blum, D. Henderson, Statistical mechanics of electrolytes at interfaces, in Fundamentals of Inhomogeneous Fluids, Marcel Dekker, Inc., 1992.

[35] M. Plischke, Pair correlation functions and density profiles in the primitive model of the electric double layer, J. Chem. Phys. 88 (1988) 2712–2718.

[36] F. J. Rogers, D. A. Young, New, thermodynamically consistent integral equation for simple fluids, Phys. Rev. A 30 (1984) 999.

[37] O. Pizio, S. Sokolowski, On the effects of ion-wall chemical association on the electric double layer: A density functional approach for the restricted primitive model at a charged wall, J. Chem. Phys 125 (2006) 024512.

[38] P. Attard, Electrolytes and the electric double layer, Adv. Chem. Phys. 92 (1996) 1–159.

[39] M. Heinen, T. Palberg, H. Lowen, Coupling between bulk and surface chemistry in suspensions of charged colloids, J. Chem. Phys. 140 (2014) 124904.

[40] J. Jiang, D. Cao, D. Henderson, J. Wu, Revisiting density functionals for the primitive model of electric double layers, J. Chem. Phys. 140 (2014) 044714.

[41] S. Carnie, D. Y. C. Chan, The structure of electrolytes at charged surfaces: Ion-dipole mixtures, J. Chem. Phys. 73 (1980) 2949–2957.

[42] S. A. Adelman, J. M. Deutch, Exact solution of the mean spherical model for strong electrolytes in polar solvents, J. Chem. Phys. 60 (1974) 3935–3949.

[43] D. Y. C. Chan, D. J. Mitchell, B. W. Ninham, B. A. Pailthorpe, On the theory of dipolar fluids and ion-dipole mixtures, J. Chem. Phys. 69 (1978) 691–696.

[44] L. Blum, D. Henderson, Mixtures of hard ions and dipoles against a charged wall: The ornstein-zernike equation, some exact results, and the mean spherical approximation, J. Chem. Phys. 74 (1981) 1902–1910.

[45] W. Dong, M. L. Rosinberg, A. Perera, G. N. Patey, A theoretical study of the solid-electrolyte solution interface. i. structure of a hard sphere ion-dipole mixture near an uncharged hard wall, J. Chem. Phys. 89 (1988) 4994.

[46] L. Perera, M. L. Berkowitz, Dynamics of ion solvation in a stockmayer fluid, J. Chem. Phys. 96 (1992) 3092–3101.

[47] F. Vericat, L. Blum, Statistical mechanics of ion-dipole mixtures: An exactly solvable model in one dimension, J. Chem. Phys. 82 (1985) 1492–1495.

[48] L. J. Frink, F. van Swol, Oscillatory surface forces: A test of the superposition approximation, J. Chem. Phys. 105 (1996) 2884–2890.

[49] R. Evans, Density Functionals in the Theory of Nonuniform Fluids, in Fundamentals of Inhomogeneous Fluids, Marcel Dekker: New York, 1992.

[50] R. Evans, The nautre of the liquid-vapour interface and other topics in the statistical mechanics of non-uniform, classical fluids, Adv. Phys. 28 (1979) 143–200.

[51] R. Evans, Density functional theory for inhomogeneous fluids i: Simple fluids in equilibrium, in Lectures at 3rd Warsaw School of Statistical Physics, Kazimierz Dolny, 2009.

[52] R. Roth, Fundamental measure theory for hard-sphere mixtures: A review, J. Phys.:Condens. Matter 22 (2010) 063102.

[53] Y. Tang, J. Wu, A density-functional theory for bulk and inhomogeneous lennard-jones fluids from the energy route, J. Chem. Phys. 119 (2003) 7388–7397.

[54] J. Wu, Z. Li, Density-functional theory for complex fluids, Ann. Rev. Phys. Chem. 58 (2007) 85–112.

[55] Y. Rosenfeld, Free-energy model for the inhomogeneous hard-sphere fluid mixture and density-functional theory of freezing, Phys. Rev. Lett. 61 (1989) 980–983.

[56] J. P. Hansen, I. R. McDonald, Theory of simple liquids, Academic Press, 1976.

[57] Y. Rosenfeld, Free energy model for the inhomogeneous hardsphere fluid: "closure" relation between generating functionals for "direct" and "cavity" distribution functions, J. Chem. Phys. 93 (1990) 4305–4311.

[58] Y. Rosenfeld, Density functional theory of molecular fluids: Free-energy model for the inhomogeneous hard-body fluid, Phys. Rev. E 50 (1994) R3318–R3321.

[59] Y. Rosenfeld, Free energy model for inhomogeneous fluid mixtures: Yukawa charged hard spheres, general interactions, and plasmas, J. Chem. Phys. 98 (1993) 8126–8148.

[60] Y. Rosenfeld, M. Schmidt, H. Lowen, P. Tarazona, Fundamental-measure free-energy density functional for hard spheres: Dimensional crossover and freezing, Phys. Rev. E 55 (1997) 4245–4263.

[61] Y. Rosenfeld, M. Schmidt, H. Lowen, P. Tarazona, Dimensional crossover and the freezing transition in density functional theory, J. Phys.:Condens. Matter 8 (1996) L577–L581.

[62] E. Kierlik, M. L. Rosinberg, Free-energy density functional for the inhomogeneous hard-sphere fluid: Application to interfactial adsorption, Phys. Rev. A 42 (1990) 3382–3387.

[63] P. Tarazona, J. A. Cuesta, Y. Martinez-Raton, Density functional theories of hard particle systems, in Theory and simulation of hard-sphere fluids and related systems, Springer, 2008.

[64] B. Medasani, Z. Ovanesyan, D. G. Thomas, M. L. Sushko, M. Marucho, Ionic asymmetry and solvent excluded volume effects on spherical electric double layers: A density functional approach, J. Chem. Phys. 140 (2014) 204510.

[65] M. Knepley, D. A. Karpeev, S. Davidovits, R. S. Eisenberg, D. Gillespie, An efficient algorithm for classical density functional theory in three dimensions: Ionic solutions, J. Chem. Phys. 132 (2010) 124101.

[66] L. J. D. Frink, F. van Swol, A molecular theory for surface forces adhesion measurements, J. Chem. Phys. 106 (1997) 3782–3791.

[67] L. J. D. Frink, F. van Swol, Solvation forces between rough surfaces, J. Chem. Phys. 108 (1998) 5588–5598.

[68] H. T. Davis, Statistical mechanics of phases, interfaces and thin films. Advances in interfacial engineering series, Wiley-VCH, 1996.

[69] T. L. Hill, Statistical thermodynamics, Dover, 1986.

[70] D. Y. C. Chan, D. J. Mitchell, B. W. Ninham, A model of solvent structure around ions, J. Chem. Phys. 70 (1979) 2946–2957.

[71] S. S. Dukhin, B. V. Derjaguin, Surface and Colloid Science, Wiley Interscience, 1974.

[72] M. K. D. Stein, C. Dekker, Surface-charge-governed ion transport in nanofluidic channels, Phys. Rev. Lett. 93 (2004) 035901.

[73] Z. S. Siwy, Ion-current rectification in nanopores and nanotubes with broken symmetry, Adv. Funct. Matter. 16 (2006) 735–746.

[74] Z. S. Siwy, I. D. Kosińska, A. Fuliński, C. R. Martin, Asymmetric diffusion through synthetic nanopores, Phys. Rev. Lett. 94 (2005) 048102.

[75] C.-P. Y. C.-C. Chang, R.-J. Yang, Ion concentration polarization near microchannel-nanochannel interfaces: Effect of ph value, Electrophoresis 33 (2012) 758–764.

[76] E. Greenfield, U. Sivan, Measuring changes in surface potential as two charged bodies approach in electrolyte solution, Phys. Rev. Lett. 102 (2009) 106101.

[77] S. Lekkala, J. A. Marohn, R. F. Loring, Electric force microscopy of semiconductors: Theory of cantilever frequency fluctuations and noncontact friction, J. Chem. Phys. 139 (2013) 184702.

[78] Y. Cui, Q. Wei, H. Park, C. M. Lieber, Nanowire nanosensors for highly sensitive and selective detection of biological and chemical species, Science 293 (2001) 1289–1292.

[79] J.-L. Hahm, C. M. Lieber, Direct ultrasensitive electrical detection of dna and dna sequence variations using nanowire nanosensors, Nano Lett. 4 (2004) 51–54.

[80] F. Patolsky, C. M. Lieber, Nanowire nanosensors, Materials Today 8 (2005) 20–28.

[81] F. Patolsky, B. P. Timko, G. Yu, Y. Fang, A. B. Greytak, G. Zheng, C. Lieber, Detection, stimulation and inhibition of neuronal signals with high-density nanowire transistor arrays, Science 313 (2006) 1100–1104.

[82] F. Patolsky, G. Zheng, O. Hayden, M. Lakadamyali, X. Zhuang, C. M. Lieber, Electrical detection of single viruses, Proc. Natl. Acad. Sci. 101 (2004) 14017–14022.

[83] F. Patolsky, G. Zheng, C. M. Lieber, Nanowire-based biosensors, Anal. Chem. 78 (2006) 4261–4269.

[84] G. Zheng, F. Patolsky, Y. Cui, W. U. Wang, C. M. Lieber, Multiplexed electrical detection of cancer markers with nanowire sensor arrays, Nature Biotechnology 23 (2005) 1294–1301.

[85] Y. Zhang, T. C. Gamble, A. Neumann, G. P. Lopez, S. R. J. Brueck, D. N. Petsev, Potential distribution and current transport in si/sio2 fluidic nanochannels, Lab on a Chip 8 (2008) 1671–1675.

[86] F. Meseguer, R. Fenollosa, I. Rodriguiez, E. Xifre-Perez, F. Ramiro-Manzano, M. Garin, M. Tymczenko, Silicon colloids: A new enabling nanomaterial, J. Appl. Phys. 109 (2011) 102424.

[87] A. Nag, M. V. Kovalenko, J.-S. Lee, W. Liu, B. Spokoyny, D. V. Talapin, Metal-free inorganic ligands for colloidal nanocrystals: S^{2-}, HS^{-}, Se^{2-}, HSe^{-}, Te^{2-}, HTe^{-}, TeS_3^{2-}, OH^{-}, and NH_2^{-} as surface ligands, J. Am. Chem. Soc. 133 (2011) 10612–10620.

[88] M. V. Kovalenko, M. I. Bodnarchuk, J. Zaumseil, J.-S. Lee, D. V. Talapin, Expanding the chemical versatility of colloidal nanocrystals capped with molecular metal chalcogenide ligands, J. Am. Chem. Soc. 132 (2010) 10085–10092.

[89] M. V. Kovalenko, M. Scheele, D. V. Talapin, Colloidal nanocrystals with metal chalcogenide surface ligands, Science 324 (2009) 1417–1420.

[90] D. V. Talapin, J.-S. Lee, M. V. Kovalenko, E. V. Shevchenko, Prospects of colloidal nanocrystals for electronic and optoelectronic applications, Chem. Rev. 110 (2010) 389–458.

[91] S.-H. Kim, S. Y. Lee, S.-M. Yang, G.-R. Yi, Self-assembled colloidal structures for photonics, NPG Asia Mater 3 (2011) 25–33.

[92] M. E. Fleharty, F. van Swol, D. N. Petsev, The effect of surface charge regulation on conductivity in fluidic nanochannels, J. Coll. Interf. Sci. 416 (2014) 105–111.

[93] M. E. Fleharty, F. van Swol, D. N. Petsev, Manipulating semiconductor colloidal stability through doping, Phys. Rev. Lett. 113 (2014) 158302.

[94] M. Borkovec, Origin of 1-pk and 2-pk models for ionizable water–solid interfaces, Langmuir 13 (1997) 2608–2613.

[95] R. J. Hunter, Zeta Potential in Colloid Science, Academic Press, New York, 1981.

[96] R. E. G. van Hal, J. C. T. Eijkel, P. Bergveld, A general model to describe the electrostatic potential at electrolyte oxide interfaces, Adv. Coll. Interf. Sci. 69 (1996) 31–62.

[97] L. G. Longsworth, Temperature dependence of diffusion in aqueous solutions, J. Phys. Chem. 58 (1954) 770–773.

[98] J. M. E. Samson, K. A. Snyder, Calculation of ionic diffusion coefficients on the basis of migration test results, Materials and Structures 36 (2003) 156–165.

[99] R. Ettelaie, R. Buscall, Electrical double layer interactions for spherical charge regulating colloidal particles, Adv. Coll. Interf. Sci. 61 (1995) 131–160.

[100] L. M. Wheeler, N. R. Neale, T. Chen, U. R. Kortshagen, Hypervalent surface interactions for colloidal stability and doping of silicon nanocrystals, Nature Comm. 4 (2013) 1–10.

[101] B. V. Derjaguin, N. V. Churaev, V. M. Muller, Surface Forces, Plenum, 1987.

[102] Y. Cui, Q. Wei, H. Park, C. M. Lieber, Nanowire nanosensors for highly sensitive and selective detection of biological and chemical species, Science 293 (2001) 1289–1292.

[103] Y. Li, F. Qian, J. Xiang, C. M. Lieber, Nanowire electronic and optoelectronic devices, Materials Today 9 (2006) 18–27.

[104] F. Patolsky, et. al., Detection, stimulation and inhibition of neuronal signals with high-density nanowire transistor arrays, Science 313 (2006) 1100–1104.

[105] F. Patolsky, et. al., Electrical detection of single viruses, Proc. Natl Acad. Sci. (USA) 101 (2004) 14017–14022.

[106] Y. Zhang, et al., Potential distribution and current transport in Si/SiO_2 fluidic nanochannels, Lab on a Chip 8 (2008) 1671–1675.

[107] S. H. Behrens, M. Borkovec, Electric double layer interaction of ionizable surfaces: Charge regulation for arbitrary potentials, J. Chem. Phys. 111 (1999) 382–385.

[108] S. L. Carnie, D. Y. C. Chan, Interaction free energy between plates with charge regulation: A linearized model, J. Colloid Interface Sci. 161 (1993) 260–264.

[109] L. D. Landau, E. M. Lifshitz, Electrodynamics of continuous media, Nauka, 1982.

[110] R. Kubo, Statistical mechanics, an advanced course with problems and solutions, North-Holland Personal Library, 2004.

[111] R. P. Feynman, N. Metropolis, E. Teller, Equations of state of elements based on the generalized fermi-thomas theory, Phys. Rev. 75 (1949) 1561.

[112] W. B. Russel, D. A. Saville, W. R. Schowalter, Colloidal Dispersions, Cambridge University Press, 1989.

[113] R. M. Mazo, Brownian motion: Fluctuations, dynamics and applications, Vol. 112, Clarendon Press, 1937.

[114] M. v. Smoluchowski, Zur kinetischen theorie der brownschen molekularbewegung und der suspensionen, Ann. Phys. (Liepzig) 21 (1906) 756–780.

[115] P. M. Debye, Reaction rates in ionic solutions, Trans. Electrochem. Soc. 82 (2942) 265–272.

[116] N. A. Fuchs, Uber der stabilitat und aufladung der aerosole, Z. Phys. (1934) 736–743.

[117] B. V. Derjaguin, V. M. Muller, Slow coagulation of hydrophobic colloids, Dokl. Akad. Nauk SSSR (in Russian) 176 (1967) 738–741.

[118] J. M. Rothberg, et al., An integrated semiconductor device enabling non-optical genome sequencing, Nature 475 (2011) 348–352.

[119] L. Shi, et al, Monodisperse silicon nanocavities and photonic cyrstals with magnetic response in the optical region, Nature Comm. 4 (2013) 1–7.

[120] S.-H. Kim, S. Y. Lee, S.-M. Yang, G.-R. Yi, Self-assembled colloidal structures for photonics, NPG Asia Mater 3 (2011) 25–33.

[121] Z. Tang, L. E. Striven, H. T. Davis, Interactions between primitive electrical double layers, J. Chem. Phys. 97 (1992) 9258.

[122] Y. X. Yu, J. Z. Wu, G. H. Gao, Density-functional theory of spherical electric double layers and zeta potentials of colloidal particles in restricted-primitive-model electrolyte solutions, J. Chem. Phys. 120 (2004) 7223–7233.

[123] L. J. D. Frink, A. G. Salinger, Two and three dimensional nonlocal density functional theory for inhomogeneous fluids i. algorithms and parallelization, J. Comp. Phys. 159(2) (2000) 407–424.

[124] Tramonto software, `https://software.sandia.gov/tramonto/`, accessed: 2014-12-29.

[125] G. A. Martynov, Power and exponential asymptotic forms of correlation functions, Theoretical and Mathematical Physics 156(3) (2008) 1356–1364.

[126] Y. Marcus, Ionic radii in aqueous solutions, Chem. Rev. 88 (1988) 1475–1498.

[127] L. J. D. Frink, F. van Swol, Solvation forces and colloidal stability - a combined monte-carlo and density-functional theory approach, J. Chem. Phys. 100 (1994) 9106–9116.

[128] J. H. Luscombe, A. M. Bouchard, Electron confinement in quantum nanostructures: Self-consistent poisson-schrodinger theory, Phys. Rev. B 46 (1992) 10262–10268.